



8-20-2018

# p62-dependent phase separation of patient-derived KEAP1 mutations and NRF2

E. W. Cloer

*University of North Carolina at Chapel Hill*

P. F. Siesser

*University of North Carolina at Chapel Hill*

E. M. Cousins

*University of North Carolina at Chapel Hill*

D Goldfarb


*University of North Carolina at Chapel Hill*

D. D. Mowrey

*University of North Carolina at Chapel Hill*

*See next page for additional authors*

Follow this and additional works at: <https://scholarlycommons.pacific.edu/cop-facarticles>

 Part of the [Biochemistry, Biophysics, and Structural Biology Commons](#), and the [Chemistry Commons](#)

## Recommended Citation

Cloer, E. W., Siesser, P. F., Cousins, E. M., Goldfarb, D., Mowrey, D. D., Harrison, J. S., Weir, S. J., Dokholyan, N. V., & Major, M. B. (2018). p62-dependent phase separation of patient-derived KEAP1 mutations and NRF2. *Molecular and Cellular Biology*, online first, DOI: [10.1128/MCB.00644-17](https://doi.org/10.1128/MCB.00644-17)  
<https://scholarlycommons.pacific.edu/cop-facarticles/567>

This Article is brought to you for free and open access by the All Faculty Scholarship at Scholarly Commons. It has been accepted for inclusion in College of the Pacific Faculty Articles by an authorized administrator of Scholarly Commons. For more information, please contact [mgibney@pacific.edu](mailto:mgibney@pacific.edu).

---

**Authors**

E. W. Cloer, P. F. Siesser, E. M. Cousins, D Goldfarb, D. D. Mowrey, Joseph S. Harrison, S. J. Weir, N. V. Dokholyan, and M. B. Major



# p62-Dependent Phase Separation of Patient-Derived KEAP1 Mutations and NRF2

E. W. Cloer,<sup>a,b</sup> P. F. Siesser,<sup>b</sup> E. M. Cousins,<sup>b</sup> D. Goldfarb,<sup>c</sup> D. D. Mowrey,<sup>d</sup> J. S. Harrison,<sup>b,d</sup> S. J. Weir,<sup>b</sup> N. V. Dokholyan,<sup>e,f</sup> M. B. Major<sup>a,b,c,g</sup>

<sup>a</sup>Department of Cell Biology and Physiology, University of North Carolina at Chapel Hill School of Medicine, Chapel Hill, North Carolina, USA

<sup>b</sup>Lineberger Comprehensive Cancer Center, University of North Carolina at Chapel Hill School of Medicine, Chapel Hill, North Carolina, USA

<sup>c</sup>Department of Computer Science, University of North Carolina at Chapel Hill, Chapel Hill, North Carolina, USA

<sup>d</sup>Department of Biochemistry and Biophysics, University of North Carolina at Chapel Hill School of Medicine, Chapel Hill, North Carolina, USA

<sup>e</sup>Department of Pharmacology, Penn State Milton S. Hershey Medical Center, Hershey, Pennsylvania, USA

<sup>f</sup>Department of Biochemistry & Molecular Biology, Penn State Milton S. Hershey Medical Center, Hershey, Pennsylvania, USA

<sup>g</sup>Department of Pharmacology, University of North Carolina at Chapel Hill School of Medicine, Chapel Hill, North Carolina, USA

**ABSTRACT** Cancer-derived loss-of-function mutations in the KEAP1 tumor suppressor gene stabilize the NRF2 transcription factor, resulting in a prosurvival gene expression program that alters cellular metabolism and neutralizes oxidative stress. In a recent genotype-phenotype study, we classified 40% of KEAP1 mutations as ANCHOR mutants. By immunoprecipitation, these mutants bind more NRF2 than wild-type KEAP1 and ubiquitylate NRF2, but they are incapable of promoting NRF2 degradation. BioID-based protein interaction studies confirmed increased abundance of NRF2 within the KEAP1 ANCHOR mutant complexes, with no other statistically significant changes to the complexes. Discrete molecular dynamic simulation modeling and limited proteolysis suggest that the ANCHOR mutations stabilize residues in KEAP1 that contact NRF2. The modeling supports an intramolecular salt bridge between the R470C ANCHOR mutation and E493; mutation of the E493 residue confirmed the model, resulting in the ANCHOR phenotype. In live cells, the KEAP1 R320Q and R470C ANCHOR mutants colocalize with NRF2, p62/SQSTM1, and polyubiquitin in structured spherical droplets that rapidly fuse and dissolve. Transmission electron microscopy coupled with confocal fluorescent imaging revealed membraneless phase-separated biomolecular condensates. We present a model wherein ANCHOR mutations form p62-dependent biomolecular condensates that may represent a transitional state between impaired proteasomal degradation and autophagy.

**KEYWORDS** KEAP1, NRF2, mutations, lung cancer, hypomorphs, clusters, biomolecular condensates, liquid-liquid phase separation, membraneless organelles, autophagy, oxidative stress, p62/SQSTM1

The National Cancer Institute projects more than 234,000 new cases of lung cancer, with mortalities in excess of 154,050 people, for 2018 (1). Lung squamous cell carcinomas (LUSC) comprise 25 to 30% of all lung cancer cases, with a 5-year survival rate of less than 5% for patients with stage IV disease, thus demonstrating a clear need for earlier diagnostic measures and novel therapeutic treatments (2–4). Comprehensive studies conducted by The Cancer Genome Atlas (TCGA) revealed mutations in the Kelch-like ECH-associated protein 1 (KEAP1) and nuclear factor erythroid 2-related

Received 1 January 2018 Returned for modification 15 January 2018 Accepted 8 August 2018

Accepted manuscript posted online 20 August 2018

**Citation** Cloer EW, Siesser PF, Cousins EM, Goldfarb D, Mowrey DD, Harrison JS, Weir SJ, Dokholyan NV, Major MB. 2018. p62-dependent phase separation of patient-derived KEAP1 mutations and NRF2. *Mol Cell Biol* 38:e00644-17. <https://doi.org/10.1128/MCB.00644-17>.

**Copyright** © 2018 American Society for Microbiology. All Rights Reserved.

Address correspondence to M. B. Major, [ben\\_major@med.unc.edu](mailto:ben_major@med.unc.edu).

factor 2 (NFE2L2; here referred to as NRF2) pathway in 34% of LUSC cases studied, underscoring the significance of this pathway in lung tumorigenesis (5).

KEAP1 functions as an intracellular sensor of oxidative stress (5–7). Under basal conditions, cytosolic KEAP1 exists as a homodimer and associates with the E3 ubiquitin ligase complex cullin-3 (CUL3) and RBX1 via a three-box motif in its broad-complex, tramtrack, bric-à-brac (BTB) domain (6–10). Dimeric KEAP1 binds two different motifs within NRF2: a high-affinity ETGE and a low-affinity DLG. These motifs bind an arginine triad motif in the KELCH domains of KEAP1 (11–14). The prevailing model is that the association of both motifs with a KEAP1 homodimer sterically positions lysine residues in NRF2 for ubiquitylation (7–11, 13). Ubiquitylated NRF2 is then delivered to the proteasome for degradation, though the precise mechanisms of this transition are unresolved. Electrophilic modifications to one or more of the 27 reactive cysteine residues in KEAP1 result in a conformational change that impairs NRF2 degradation (15–19). Consequently, in the absence of free homodimeric KEAP1, *de novo*-synthesized NRF2 accumulates and translocates to the nucleus (11, 20, 21). Nuclear NRF2 heterodimerizes with small Maf proteins and binds to antioxidant response elements (ARE)/electrophile response elements (EpRE) in the promoters of target genes, including the phase II detoxifying enzyme NAD(P)H dehydrogenase [quinone] 1 gene (*NQO1*), glutathione synthesis genes, and heme oxygenase 1 gene (*HMOX1*) (20–22).

Live-cell imaging studies utilizing fluorescence lifetime imaging (FLIM) coupled with Förster resonance transfer (FRET) constructs established that KEAP1 cycles between two distinct conformations: open and closed (15). Initially, KEAP1 exists in the cytosol as a homodimer with a 1:1 stoichiometry with the CUL3 complex (15, 23, 24). As NRF2 protein levels increase, KEAP1 binds the ETGE motif of NRF2, thus establishing the open conformation of the KEAP1-NRF2 complex (15). Binding of the low-affinity DLG motif generates the closed conformation of the complex, in which ubiquitylation of NRF2 is sterically favorable (15). The closed complex delivers ubiquitylated NRF2 to the proteasome for degradation, and removal of the ubiquitylated substrate results in regeneration of free and open KEAP1, enabling cycling to continue (15). Reactive oxygen species and electrophilic compounds modify KEAP1 conformation, resulting in impaired cycling and accumulation of the closed KEAP1-NRF2 complex (15). In order to reestablish redox-sensing capabilities, cells must regenerate free KEAP1 and remove KEAP1-NRF2 closed complexes; the mechanism of how this occurs has yet to be fully elucidated (15, 25–27).

Due to its essential role in mitigating oxidative stress, a delicate balance of KEAP1-NRF2 signaling is required to maintain cellular homeostasis. Inappropriately low or high NRF2 activity is associated with a variety of disease conditions (5, 16, 28, 29). Diminished or absent NRF2 activity is associated with an increased risk for neurodegeneration and aging (16, 30, 31). In contrast, prolonged periods of NRF2 hyperactivation correlate with an increased risk for tumorigenesis (31–34). In greater than 30% of lung cancers, mutations in KEAP1 or NRF2 contribute to constitutive NRF2 activity, which correlates with increased resistance to chemotherapy and poor patient outcome (5, 10, 31, 32, 35–37).

Although over 700 somatic mutations in KEAP1 have been identified in cancer, the mechanism and functional consequences of the majority of these mutations remain unknown (38, 39). Analysis of 178 LUSC patients directed by the TCGA Consortium revealed 18 mutations in KEAP1 (5). To determine the functional significance of these mutations in LUSC, we cloned and profiled the mutants to define their impact on NRF2 function and biochemical activity (40). From these data, we identified three distinct functional classes: (i) silent mutations which most likely represent passenger events, (ii) hypomorphic mutations, and (iii) functionally dead proteins (40). Further interrogation of the hypomorphic mutant class revealed seven mutations which exhibit increased binding to NRF2 by immunoprecipitation yet lack the ability to suppress NRF2 transcription (40). Here we refer to this class of KEAP1 mutations as ANCHOR mutants (additionally NRF2-complexed hypomorph). These ANCHOR mutations were previously referred to as superbinders; however, because binding affinities remain to be defined,

the term superbinder was replaced with ANCHOR for clarity. Remarkably, cell-based and *in vitro* studies determined that the KEAP1 R320Q ANCHOR mutation retains the ability to ubiquitylate NRF2 (40).

From our analyses of the LUSC KEAP1 mutations, we estimate that KEAP1 ANCHOR mutations represent more than one-third of patient-derived LUSC KEAP1 mutations. In this study, we examined the mechanism and phenotypic consequences of the ANCHOR mutants. Proximity-based proteomic analyses of KEAP1 ANCHOR complexes revealed exclusive enrichment of NRF2, with minimal impact on other KEAP1-associated proteins. Structural molecular dynamic simulations and biochemical studies suggest that ANCHOR mutants stabilize KEAP1 tertiary structure, particularly at interfacing residues with NRF2. In cells, ANCHOR mutants form spherical clusters containing polyubiquitin, the autophagy cargo adaptor p62/SQSTM1 (p62), KEAP1, and NRF2. The formation of these clusters is p62 dependent, yet surprisingly, the clusters are not cleared by autophagy. Live-cell imaging and transmission electron microscopy (TEM) establish the clusters as membraneless organelles with liquid-like properties, defining features of biomolecular condensates. As expected, overexpression of KEAP1 ANCHOR mutants protects cells from DNA damage. Together, these studies provide new insight into the function of KEAP1 ANCHOR mutations.

## RESULTS

**The mutational landscape of NRF2 and KEAP1.** Across many cancer types, inactivating mutations in KEAP1 and activating mutations in NRF2 are mutually exclusive. Further, KEAP1 mutations lack positional enrichment, whereas mutations in NRF2 localize to the KEAP1 binding sites, features that are consistent with tumor suppressor and oncogene functions, respectively (5, 38, 40–48). To illustrate these patterns, we compiled mutation data from cBioPortal into kernel density estimation (KDE) plots (Fig. 1A and B; see also Tables S1 and S2 in the supplemental material) (38, 39). In NRF2, 448 mutations localize almost exclusively to the DLG and ETGE motifs, which are required for binding to KEAP1 (Fig. 1A) (40). In contrast, the 718 mutations identified in KEAP1 lack appreciable focal enrichment (Fig. 1B) (5, 38, 40, 43). Known ANCHOR mutations also do not colocalize within KEAP1. Two of the three most frequently mutated residues in KEAP1 are R320 and R470, and mutations to both of these residues result in an ANCHOR phenotype (Fig. 1B) (40).

We hypothesized that functionally relevant mutations in NRF2 and KEAP1 would occur more frequently at evolutionarily conserved amino acid residues compared to passenger mutations or nonmutated residues. To test this, we examined the correlation between mutational frequency (MF) and evolutionary conservation as estimated by Shannon entropy (SE) for a given amino acid residue (Fig. 1C to F) (38, 49, 50). MF-versus-SE plots for NRF2 and KEAP1 revealed a general trend of cancer-derived mutations affecting evolutionarily conserved residues (Fig. 1C and D). For both NRF2 and KEAP1, the difference between SE for nonmutated and mutated residues was statistically significant (Fig. 1E and F). Therefore, these data contribute to previous studies which demonstrated evolutionary conservation of oncogenic mutations in tumor suppressors and oncogenes, including TP53 (51, 52). Although multiple amino acid substitutions are observed at the ANCHOR residues R320 and R470, we chose to further characterize the R320Q and R470C mutations identified in the TCGA LUSC data set (5).

**Biochemical characterization of the KEAP1 ANCHOR mutants.** To explore the mechanism of the ANCHOR mutants, we examined NRF2 stability and KEAP1-NRF2 association. We first probed the dynamics of NRF2 stabilization using live-cell imaging. HEK 293T/17 cells transiently overexpressing murine EGFP-Nrf2 (mEGFP-Nrf2) or human Venus-NRF2 (Venus-NRF2) were monitored every hour for 24 h, and NRF2 stabilization was plotted as a function of green fluorescence intensity. Analysis of fluorescent NRF2 intensity confirmed that KEAP1 R320Q and R470C rapidly stabilized NRF2 within hours of transfection (Fig. 2A); similar stabilization was observed in H1299 lung adenocarcinoma cells (data not shown). NRF2 stabilization in the presence of KEAP1 R320Q

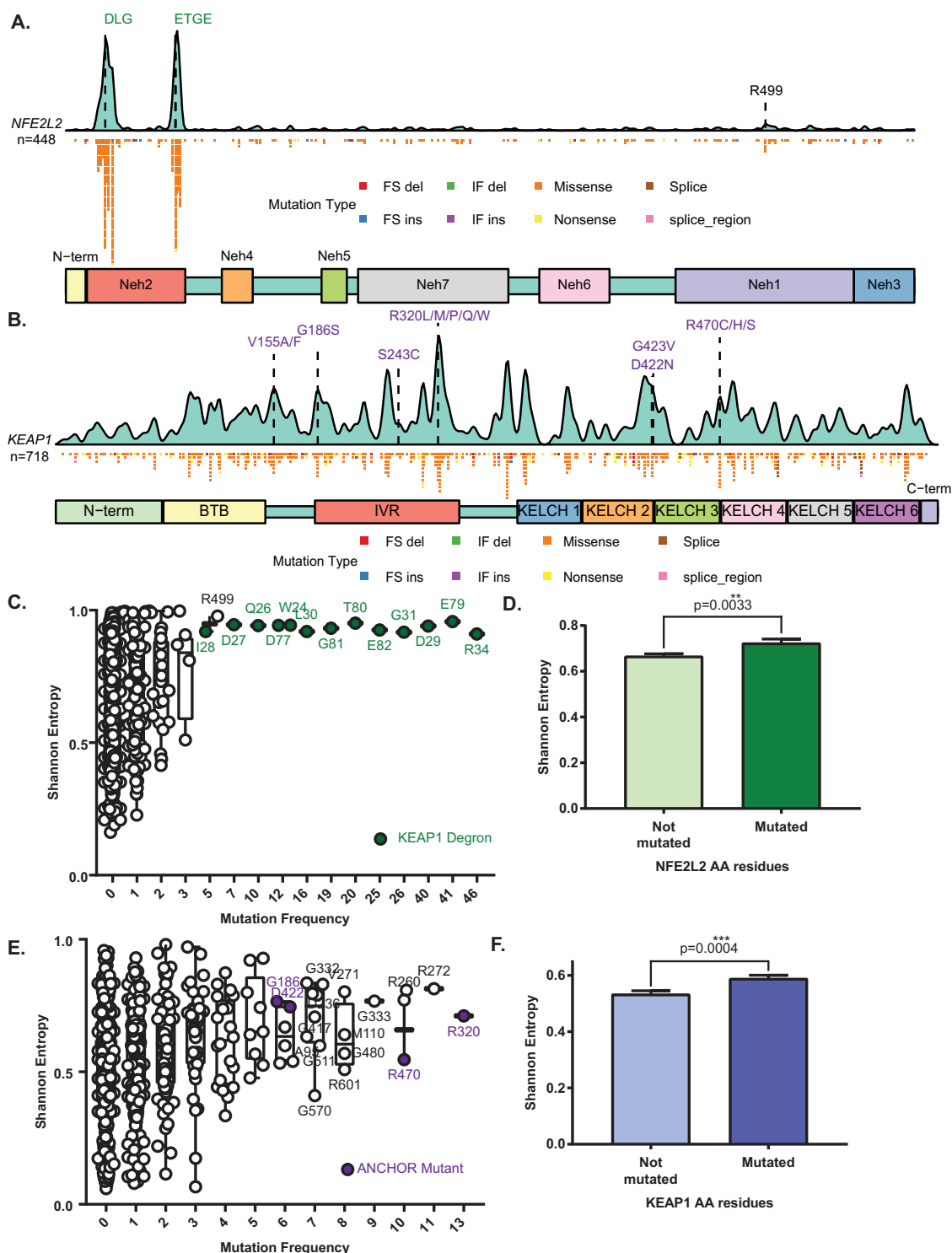


**FIG 1** Defining the mutational landscape of NRF2 and KEAP1. (A) Kernel density estimation (KDE) of 448 NRF2 somatic mutations demonstrates focal enrichment of mutations at the DLG and ETGE motifs, which are required for KEAP1 association. Fourteen patients exhibited in-frame deletions across the DLG and/or ETGE; five patients had *NFE2L2* intragenic fusion events, and one patient had a *ZNF385B-NFE2L2* fusion. Data from these patients were not included in the KDE analysis; only missense mutations were used to compute the KDE. Data were downloaded from cBioPortal and represent *NFE2L2* mutations across 59 studies investigating 37 different cancer types (Table S1) (38, 39). (B) KDE of 718 KEAP1 somatic mutations identified in patient samples reveals elevated mutational frequencies at ANCHOR residues R320 and R470. Data were downloaded from cBioPortal and represent *KEAP1* mutations across 68 studies investigating 33 different cancer types (Table S2) (38, 39). (C) Plot of NRF2 mutational frequency versus Shannon entropy. Shannon entropy was calculated from the PROMALS3D sequence alignment, and mutational frequencies per residue were determined from cBioPortal data (Table S3). (D) Comparison of Shannon entropy values for all nonmutated residues in NRF2 ( $n = 459$ ) versus mutated residues ( $n = 146$ ). Error bars represent the standard error of the mean (SEM). The difference is statistically significant at  $p=0.0033$ . (E) Plot of KEAP1 mutational frequency versus Shannon entropy. Shannon entropy was calculated from the PROMALS3D sequence alignment, and mutational frequencies per residue were determined from cBioPortal data (Table S3). (F) Comparison of Shannon entropy values for all nonmutated residues in KEAP1 ( $n = 68$ ) versus mutated residues ( $n = 13$ ). Error bars represent the standard error of the mean (SEM). The difference is statistically significant at  $p=0.0004$ . (Continued on next page)

overexpression was also observed in HEK 293T/17 cells using immunofluorescence (IF) (Fig. S1A).

Next, we compared KEAP1-NRF2 association using two complementary approaches: immunopurification followed by Western blotting (IP/W.blot) and proximity ligation assay (PLA). Analysis of IP/W.blot for FLAG-KEAP1 complexes from HEK 293T/17 cells demonstrated that with the exception of G423V and G186R, the ANCHOR mutants were expressed comparably to the wild type (WT). Furthermore, all ANCHOR mutants stabilized endogenous NRF2 in the total cell lysate (Fig. 2B, lanes 3 to 9), although not to the same extent as WT KEAP1 treated with the proteasome inhibitor MG-132 (Fig. 2B, lanes 10, 20, and 30). Analysis of the immunopurified complex demonstrated increased association of NRF2 with all seven ANCHOR mutants (Fig. 2B, lanes 13 to 19) and increased NRF2 protein levels in the unbound fraction (Fig. 2B, lanes 23 to 29). Not all ANCHOR mutants are functionally equivalent; examination of the bound NRF2 suggests that there are two distinct classes of ANCHOR mutants (Fig. 2B). In the first class, the R320Q, R470C, D422N, and G186R mutants consistently bound more NRF2 than the second ANCHOR class, consisting of the G423V, S243C, and V155F mutants (Fig. 2B, compare lanes 13, 14, 16, and 17 with lanes 15, 18, and 19).

To determine localization and to further quantify KEAP1-NRF2 complex formation, PLA (53, 54) was employed. Consistent with reported literature, confocal imaging analysis of the PLA puncta demonstrated KEAP1-NRF2 complex formation primarily within the cytosol (Fig. 2C) (15, 18, 23–25, 53, 54). Quantification of the PLA signal confirmed a >2-fold increase in R320Q KEAP1-NRF2 complex formation compared to that with the WT (Fig. 2D). To confirm the increased association of NRF2 with KEAP1 ANCHOR mutants in a more clinically relevant cell line, we performed PLA with H1299 lung adenocarcinoma cells. PLA of KEAP1 R320Q and R470C with endogenous NRF2 demonstrated increased KEAP1-NRF2 complex formation within the cytosol of the cell compared to that with the WT (Fig. 2E). Additionally, we compared the stabilization of the KEAP1-NRF2 complex in the presence of the ANCHOR mutants with a panel of NRF2 inducers: sulforaphane (SFN), bardoxolone-methyl (CDDO), MLN4924, and MG-132 (55, 56). The neddylation inhibitor MLN4924 was the most robust inducer of the NRF2-KEAP1 PLA signal (Fig. 2E and F) (55, 56). Cysteine-modifying compounds SFN and CDDO also stabilized the KEAP1-NRF2 complex but to a lesser extent than MLN4924 (19, 57–59). Moreover, the R320Q and R470C mutants stabilized the KEAP1-NRF2 interaction comparably to treatment with the proteasomal inhibitor MG-132 (Fig. 2F; see also Fig. S1D) (60). IF and WB were used to confirm equivalent expression of the FLAG-KEAP1 constructs as well as to assess NRF2 stabilization in H1299 cells (Fig. S1B to D).

**Defining protein-protein interactions of KEAP1 ANCHOR mutants.** Substrates targeted for ubiquitylation are often low-abundance proteins or have transient interactions that are difficult to detect by traditional immunopurification mass spectrometry (IP/MS); therefore, we employed an unbiased MS approach to probe for additional KEAP1 substrates and/or interacting proteins with altered association with the ANCHOR mutants. BioID is a technique employing the use of a modified promiscuous biotin ligase (BirA\*) fused to a bait protein (61–63). Proteins that associate proximally with the bait are biotinylated by the ligase and can be affinity purified using streptavidin and detected by MS or W.blot analyses (61–63). Biotinylated complexes from HEK 293T/17 cells stably overexpressing BirA\*-KEAP1 WT, R320Q, or R470C were affinity purified using streptavidin, and eluted peptides were analyzed using liquid chromatography-mass spectrometry (LC-MS/MS). Proteomic analyses revealed NRF2 as the only protein significantly increased within KEAP1 R320Q protein complexes (Fig. 3A). NRF2 was also significantly increased within KEAP1 R470C protein complexes (Fig. S2A).

#### FIG 1 Legend (Continued)

$P = 0.0033$  using an unpaired  $t$  test. (E) Plot of KEAP1 mutational frequency versus Shannon entropy. Data were analyzed as for panel C (Table S4). (F) Comparison of Shannon entropy values for all nonmutated residues ( $n = 306$ ) in KEAP1 versus mutated residues ( $n = 318$ ). Error bars represent SEMs. The difference is statistically significant at a  $P$  value of 0.0004 using an unpaired  $t$  test.



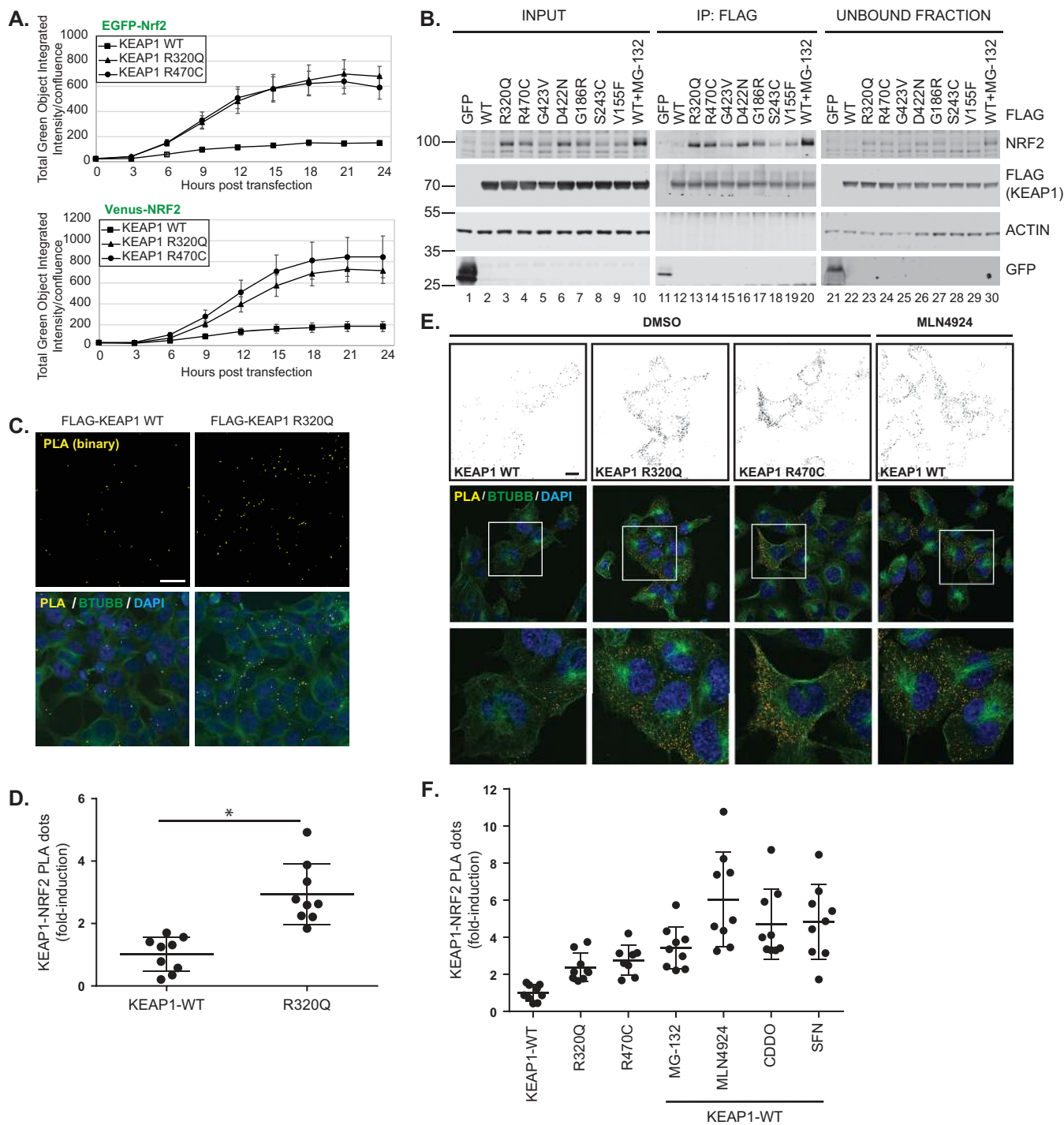


**FIG 2** KEAP1 ANCHOR mutants stabilize NRF2 and increase KEAP1-NRF2 association. (A) HEK 293T/17 cells were cotransfected with FLAG-KEAP1 WT, R320Q, or R470C and either EGFP-Nrf2 or Venus-NRF2 and immediately subjected to image acquisition using the InCuCyte Zoom. GFP and phase images were acquired every hour at 20 $\times$  with four fields/well. Data were plotted every 3 h, and total green object integrated intensity values were normalized by percentage confluence. Each graph represents the average from three biological replicates, with four technical replicates per condition for each experiment. Error bars represent standard errors from triplicates. (B) IP/W-blot of HEK 293T/17 cells transfected with indicated FLAG-KEAP1 constructs. At 18 h posttransfection, cells were treated with DMSO or 10  $\mu$ M MG-132 for 6 h prior to harvest. Data are representative of those from a single experiment performed in biological triplicate. (C) HEK 293T/17 cells stably expressing FLAG-KEAP1 WT or R320Q were subjected to PLA using FLAG and NRF2 antibodies for detection of overexpressed KEAP1 and endogenous NRF2 interactions (yellow). Images represent maximum intensity projections of Z-stacks acquired using a confocal microscope. For clarity, both color and black-and-white images of the PLA dots are provided. Nuclei were stained with DAPI (blue), and microtubules were counterstained with antitubulin antibody (green). Scale bar = 20  $\mu$ m. (D) Fold induction relative to WT of KEAP1-NRF2 interaction in cells expressing R320Q. PLA dots were quantified and normalized by cell number prior to calculation of fold induction. Data are presented as means  $\pm$  SDs. \*,  $P < 0.001$ . Data are representative of those from a single experiment performed in biological triplicate. (E) H1299 cells were transfected with FLAG-KEAP1 WT, R320Q, or R470C. The following day, cells were treated with either DMSO (control) or a panel of NRF2 inducers—10  $\mu$ M MG-132, 5  $\mu$ M MLN4924, 375 nM CDDO, 50  $\mu$ M tBHQ, or 20  $\mu$ M SFN—for 6 h. Cells were then (Continued on next page)



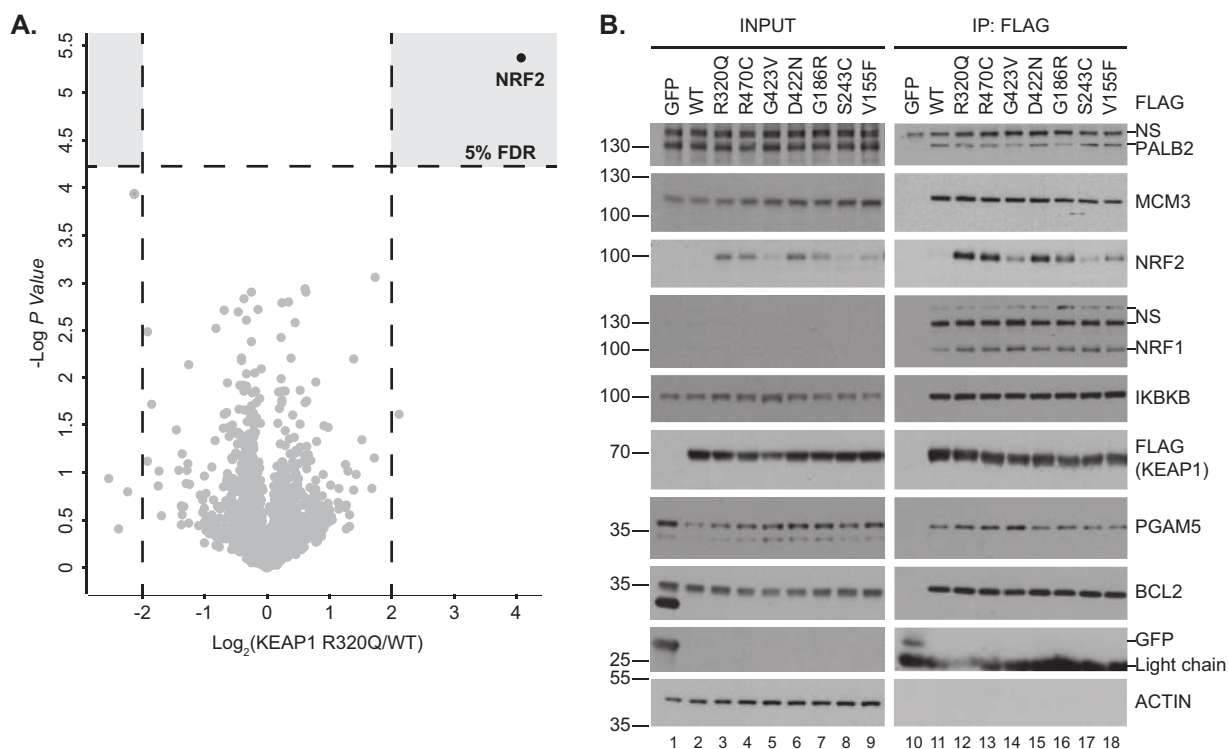


**FIG 3** NRF2 is the only KEAP1 substrate to exhibit an ANCHOR phenotype. (A) Volcano plot of BirA\*-KEAP1 R320Q versus BirA\*-KEAP1 WT. Experiments were performed in biological triplicate using HEK 293T/17 cells stably expressing BirA\*-KEAP1 WT or R320Q and treated with 50  $\mu$ M biotin for 24. Biotinylated proteins were affinity purified using streptavidin, and the bound complexes were subjected to LC-MS/MS. Dashed vertical lines indicate a 4-fold change cutoff. The horizontal dashed line indicates a 5% FDR threshold, determined using the permutation test implemented in Perseus. *P* values were determined using the two-tailed *t* test. (B) IP/W.blot of HEK 293T/17 cells transiently transfected with the indicated FLAG-KEAP1 constructs. FLAG-KEAP1 complexes were immunopurified and probed for endogenous substrate proteins as indicated. Data are representative of those from a single experiment performed in biological triplicate.

To evaluate known KEAP1 substrates, IP/W.blot for all putative substrates was performed. IP/W.blot from HEK 293T/17 cells overexpressing FLAG-KEAP1 WT or all seven ANCHOR mutants confirmed that only NRF2 association increased with KEAP1 ANCHOR overexpression (Fig. 3B). Of the substrates examined, significant stabilization of PALB2, MCM3, NRF1, IKBKB, or BCL2 in the input or in the bound complex was not observed (Fig. 3B) (64–72). In contrast, PGAM5 stabilization was observed in the input with KEAP1 ANCHOR mutants (Fig. 3B, compare lane 2 with lanes 3 to 9); however, excluding G423V, PGAM5 association did not increase significantly with KEAP1 ANCHOR overexpression (Fig. 3B, compare lane 11 with lanes 12 to 18). NRF1 and PGAM5 antibodies were confirmed using small interfering RNAs (siRNAs) (Fig. S2B and C). Endogenous NRF1 protein levels were undetectable in the lysate but were detectable following MG-132 treatment (Fig. 3B; see also Fig. S2B and C).

**Probing mechanistic steps in KEAP1 cycling.** Our data indicate that KEAP1 ANCHOR mutants stabilize NRF2 while maintaining NRF2 ubiquitylation, suggesting that ANCHOR mutants may impair KEAP1 cycling or substrate release to the proteasome (40). To test this hypothesis, different biochemical steps of the cycling process were systematically evaluated. We first confirmed that KEAP1 ANCHOR mutants can homodimerize by overexpressing N-terminally tagged streptavidin-binding peptide and hemagglutinin-tagged KEAP1 (pIRESpuro-GLUE-KEAP1; here pGLUE-KEAP1) and

#### FIG 2 Legend (Continued)

fixed and subjected to PLA using FLAG and NRF2 antibodies for detection of KEAP1 interactions with endogenous NRF2 (yellow). Images represent a single optical slice acquired using a confocal microscope as for panel C. Scale bar = 20  $\mu$ m. (F) Fold induction relative to WT of KEAP1-NRF2 interaction in cells expressing untreated WT, the R320Q or R470C mutant, or NRF2 inducer-treated WT. PLA dots were quantified and normalized by cell number prior to calculation of fold induction. Data are presented as means  $\pm$  SDs. Data are representative of those from a single experiment performed in biological triplicate.

FLAG-KEAP1 in *Keap1*<sup>-/-</sup> mouse embryonic fibroblasts (MEFs). These experiments were conducted with a KEAP1 null cell line to eliminate potential contributions from endogenous KEAP1. First, IP/W.blot demonstrated that KEAP1 ANCHOR mutants retain the ability to homodimerize (Fig. 4A). Second, KEAP1/CUL3 association was also examined using transient overexpression of FLAG-KEAP1 ANCHOR mutants in *Keap1*<sup>-/-</sup> MEFs. IP/W.blot analyses confirmed that KEAP1 ANCHOR mutants associate with CUL3 comparably to KEAP1 WT (Fig. 4B). Third, given the previously reported interaction between KEAP1 and the proteasomal chaperone HSP90, the interaction between KEAP1 WT or R320Q and HSP90 was assessed (40, 73). Interactions between HSP90 and KEAP1 WT or R320Q were not observed (Fig. S3A) (40, 73).

A recent report details the mechanism by which p97/valosin-containing protein (VCP) and cofactors UFD1/NPL4 and UBXN7 remove ubiquitylated NRF2 from the KEAP1-CUL3 complex for proteasomal delivery (27). These data were consistent with our hypothesis that KEAP1 ANCHOR mutants impair proteasomal degradation downstream of ubiquitylation but prior to proteolysis; consequently, interaction between KEAP1 and VCP was examined (27). In both HEK 293T/17 cells and *Keap1*<sup>-/-</sup> MEFs, we observed that KEAP1 WT, R320Q, and R470C bind VCP; however, no appreciable difference in VCP association between KEAP1 WT and the two ANCHOR mutants was detected (Fig. 4C and D). Treatment with VCP inhibitors CB-5083, DBE-Q, and Eeyrestatin 1 (Eey1) modestly reduced VCP levels, with no effect on KEAP1 or NRF2 levels (Fig. 4E, lanes 2 to 4 and 7 to 9) or association with KEAP1 WT or R320Q (Fig. 4E, lanes 12 to 14 and 17 to 19) (74–77). Finally, MG-132 treatment had no impact on VCP or KEAP1 levels or association (Fig. 4E, lanes 5, 10, 15, and 20). VCP siRNAs were used to validate the VCP antibody (Fig. S3B).

To test KEAP1 association with the proteasome, IP/W. blot for ubiquitin receptors PSMD2 and PSMD4 was performed (78–85). IP/W.blot of FLAG-KEAP1 WT, R320Q, or R470C demonstrated no differences in association with either PSMD2 or PSMD4 between KEAP1 WT or the ANCHOR mutants (Fig. 4F, lanes 7 to 9). Treatment with MG-132 did not lead to increased association of KEAP1 WT with either PSMD2 or PSMD4 (Fig. 4F, lane 10). From these data, we conclude that aside from NRF2, ANCHOR mutations do not impact KEAP1 protein-protein interactions.

**Assessing KEAP1 ANCHOR structure.** Modifications to cysteines within KEAP1 are thought to alter KEAP1 architecture, thus impeding ubiquitin-dependent proteolysis of substrates (19, 28, 59, 86). Mutations impacting cysteine reactivity or causing structural deformation of KEAP1 could result in the ANCHOR phenotype. The lack of an available full-length crystal structure for KEAP1 precluded molecular modeling to determine how R320Q impacts KEAP1 structure; however, molecular modeling and simulations of the KEAP1 KELCH domain could be used to investigate how the R470C ANCHOR mutation may impact KEAP1 structure when complexed with NRF2.

Discrete molecular dynamics (DMD) simulation demonstrated that the R470C mutation significantly reduced root mean square fluctuations (RMSF) of several residues between amino acid numbers 500 and 550 (Fig. 5A) (87–90). A decrease in RMSF corresponds to reduced motion, suggesting that the R470C mutation has a stabilizing effect on these residues. When mapped to the crystal structure, decreases in RMSF were observed to propagate throughout the KEAP1 KELCH domain and to contact loops with the NRF2 degron (Fig. 5B).

To further confirm the effects of KEAP1 ANCHOR mutations on KEAP1 tertiary structure, low-resolution limited trypsin proteolysis was performed (91). Lysates from *Keap1*<sup>-/-</sup> MEFs transiently overexpressing FLAG-KEAP1 WT, R320Q, or R470C were exposed to increasing concentrations of trypsin. Although the molecular weight banding patterns generated by trypsin were similar for the WT and the two ANCHOR mutants, the intensity for bands between 50 and 70 kDa differed between KEAP1 WT and the ANCHOR mutants. More specifically, the R320Q and R470C mutants were more resistant to tryptic proteolysis than was KEAP1 WT (Fig. 5C, compare lanes 4 and 5 with

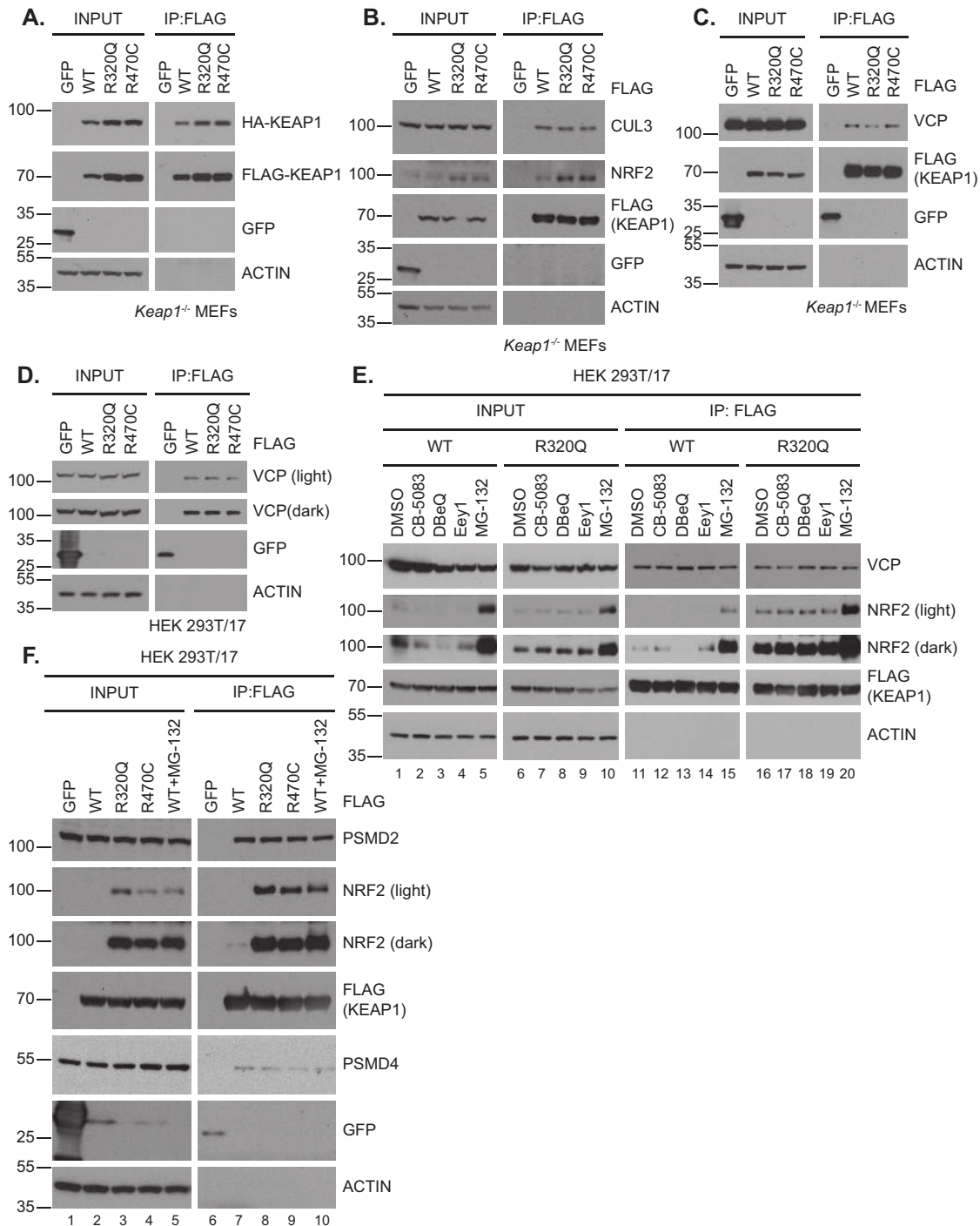


**FIG 4** KEAP1 ANCHORS R320Q and R470C exhibit biochemical interactions similar to those of KEAP1 WT. (A) IP/W.blot of *Keap1*<sup>-/-</sup> MEFs transiently cotransfected with the indicated FLAG-KEAP1 and pGLUE-KEAP1 constructs. FLAG-KEAP1 complexes were immunopurified and probed for HA-KEAP1 to determine homodimerization. Data are representative of a single experiment performed in biological triplicate. (B) IP/W.blot of *Keap1*<sup>-/-</sup> MEFs transiently transfected with the indicated FLAG-KEAP1 constructs. FLAG-KEAP1 complexes were immunopurified and probed for association with endogenous CUL3. Data are representative of those from a single experiment performed in biological triplicate. (C and D) IP/W.blot of *Keap1*<sup>-/-</sup> MEFs or HEK 293T/17 cells transiently transfected with the indicated FLAG-KEAP1 constructs. FLAG-KEAP1 complexes were immunopurified and probed for association with endogenous VCP. Data are representative of those from a single experiment performed in biological triplicate. (E) IP/W.blot of HEK 293T/17 cells transiently transfected with the indicated FLAG-KEAP1 constructs. Cells were treated with 1  $\mu$ M CB-5083, 10  $\mu$ M DBEq, 10  $\mu$ M Eey1, or 10  $\mu$ M MG-132 for 6 h. Data are representative of those from a single experiment performed in biological duplicate. (F) IP/W.blot of HEK 293T/17 cells transiently transfected with the indicated FLAG-KEAP1 constructs. Cells were treated with 10  $\mu$ M MG-132 for 6 h. FLAG-KEAP1 complexes were immunopurified and probed for association with ubiquitin receptors. Data are representative of those from a single experiment performed in biological triplicate.

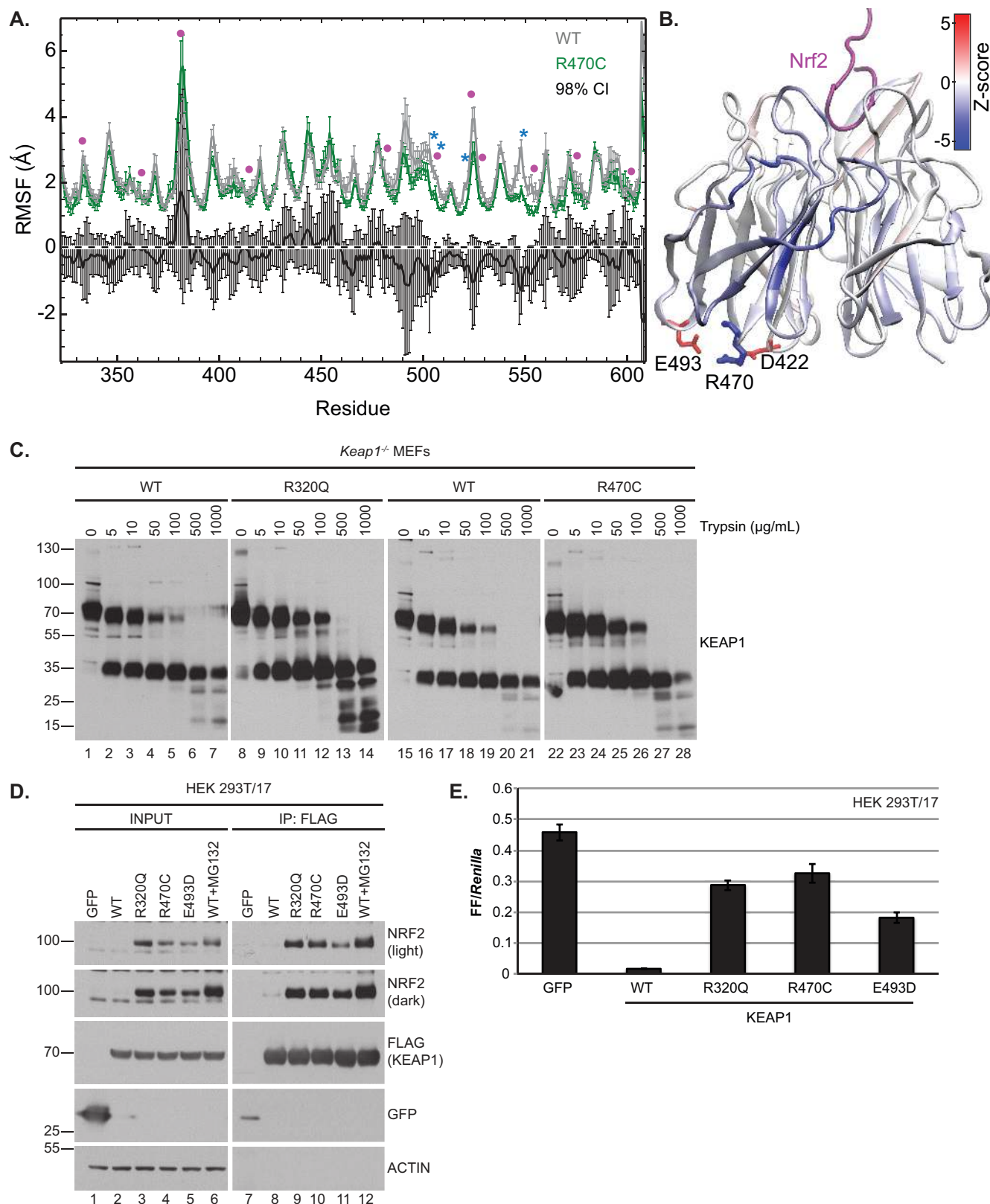


**FIG 5** KEAP1 ANCHOR mutants stabilize KEAP1 structure. (A) Plot of the root mean square fluctuations (RMSF) at each residue for KEAP1 WT (gray) and R470C (green). For each system, the mean and standard error of five replicates, each with one million steps, were plotted. Magenta circles denote the contact points with Nrf2 in the crystal structure (PDB code 4IFL). The black line corresponds to the difference between the means for R470C and WT simulations, and error bars correspond to the 98% confidence intervals (CI) for the differences between the means. Blue asterisks indicate statistically significant decreases in RMSF ( $P < 0.02$ ). (B) Cartoon representation of the KEAP1-Nrf2 crystal structure colored by the Z-score for the RMSF difference between KEAP1 mutant and WT. The

(Continued on next page)

lanes 11 and 12). These limited-proteolysis experiments suggest that R320Q and R470C alter the structure of KEAP1, a finding that is consistent with the DMD simulations.

Examination of potential interactions with R470 revealed two acidic residues, D422 and E493, that are capable of forming a salt bridge with R470 (Fig. 5B). Interestingly, mutation of D422 also results in an ANCHOR phenotype (Fig. 2B, lanes 6 and 16) (40); therefore, we hypothesized that mutations to E493 may also result in an ANCHOR phenotype. Analysis of cBioPortal data revealed a lung squamous cell carcinoma patient (TCGA-18-5595-01) harboring a KEAP1 E493D mutation (38, 39). IP/W.blot of the KEAP1 E493D mutation demonstrated stabilization of NRF2 in the whole-cell lysate comparable to that with KEAP1 R320Q and R470C (Fig. 5D, compare lane 5 with lanes 3 and 4). Similarly, KEAP1 E493D bound NRF2 comparably to KEAP1 R320Q and R470C (Fig. 5D, compare lane 11 with lanes 9 and 10). To determine the effect of the KEAP1 E493D mutation on NRF2 transcriptional activation, we used the hQR41-ARE luciferase assay (92). The KEAP1 E493D mutant exhibited hypomorphic suppression of NRF2 transcriptional activity consistent with the ANCHOR class of mutations (Fig. 5E) (40).

KEAP1 stability and ubiquitylation were also assessed. Cycloheximide (CHX) chase experiments under basal and oxidative stress-inducing *tert*-butylhydroquinone (tBHQ) conditions confirmed that KEAP1 R320Q does not alter KEAP1 half-life (Fig. S4A and B) (93, 94). IP/W.blot for ubiquitylated KEAP1 under native conditions demonstrated that KEAP1 ANCHOR mutants did not alter KEAP1 ubiquitylation under basal or induced (tBHQ and MG-132) conditions (Fig. S4C, lanes 15 and 16, 19 and 20, and 23 and 24), nor did they alter KEAP1 K48 or K63 ubiquitin chain formation (Fig. S4D, lanes 11 to 16). KEAP1 K48 ubiquitylation was further confirmed under near denaturing conditions using an antibody for endogenous K48 ubiquitin (Fig. S4E, lanes 6 to 8).

**KEAP1 ANCHOR mutants form p62-dependent biomolecular condensates.** The proposed impairment to KEAP1 structure led us to investigate KEAP1 localization in the presence of the ANCHOR mutants. Fluorescently tagged constructs were used to visualize the KEAP1-NRF2 complex in real time (15). We first tested subcellular localization by independently overexpressing murine enhanced green fluorescent protein-Nrf2 (mEGFP-Nrf2) or murine Keap1-mCherry (mKeap1-mCh) WT, R320Q, or R470C. Consistent with recent reports, mEGFP-Nrf2 localized primarily to the nuclear compartment in HEK 293T/17 and H1299 cells, with nuclear foci observed in H1299 (Fig. S5A and B). In contrast, each of the mKeap1-mCh constructs resulted in a diffuse cytosolic subcellular localization, with increased Keap1-positive clusters observed in H1299 cells compared to HEK293T/17 cells (Fig. S5A and B) (15). Next, overexpression of mEGFP-Nrf2 in the presence of mKeap1 WT, R320Q, or R470C was examined. A distinct increase in Keap1-Nrf2-containing clusters was observed when mEGFP-Nrf2 was overexpressed in the presence of the ANCHOR mutants in both HEK 293T/17 and H1299 cells (Fig. 6A; see also Fig. S5C).

Cytoplasmic inclusions are characterized by insoluble protein aggregates; thus, the Triton X-100 solubility assay was used to complement the fluorescence microscopy data (95). Similar accumulations within the insoluble fractions for all of the FLAG-KEAP1 constructs were observed (Fig. 6B, lanes 12 to 14). However, NRF2 accumulation within the insoluble fraction occurred only in the presence of R320Q and R470C or with KEAP1 WT treated with MG-132 (Fig. 6B, lanes 12 to 15).

Insoluble inclusion bodies and aggregate structures are often a hallmark of autophagy, a bulk cellular recycling pathway involved in protein homeostasis (96–99). KEAP1 binds the autophagy ubiquitin cargo adaptor p62/SQSTM1 (p62) via a KEAP1

#### FIG 5 Legend (Continued)

bound NRF2 peptide is colored magenta. The mutated residue R470 and the potential salt bridge partners are shown as sticks (red, acidic residues; blue, basic residues). (C) W.blot of lysates from limited proteolysis of *Keap1*<sup>-/-</sup> MEFs transiently transfected with FLAG-KEAP1 constructs and exposed to various concentrations of trypsin for 15 min. (D) IP/W.blot of HEK 293T/17 cells transiently transfected with the indicated FLAG-KEAP1 constructs. Cells were treated with 10  $\mu$ M MG-132 for 6 h. FLAG-KEAP1 complexes were immunopurified and probed for association with the indicated proteins. Data are representative of those from a single experiment performed in biological triplicate. (E) hQR41-ARE luciferase assay of HEK 293T/17 cells transiently transfected with the indicated FLAG-KEAP1 constructs. Data are presented as the average ratios of firefly (FF) to *Renilla* luciferase, with error bars representing SEMs across six technical replicates. Data are representative of 5 biological replicates performed by two independent researchers.



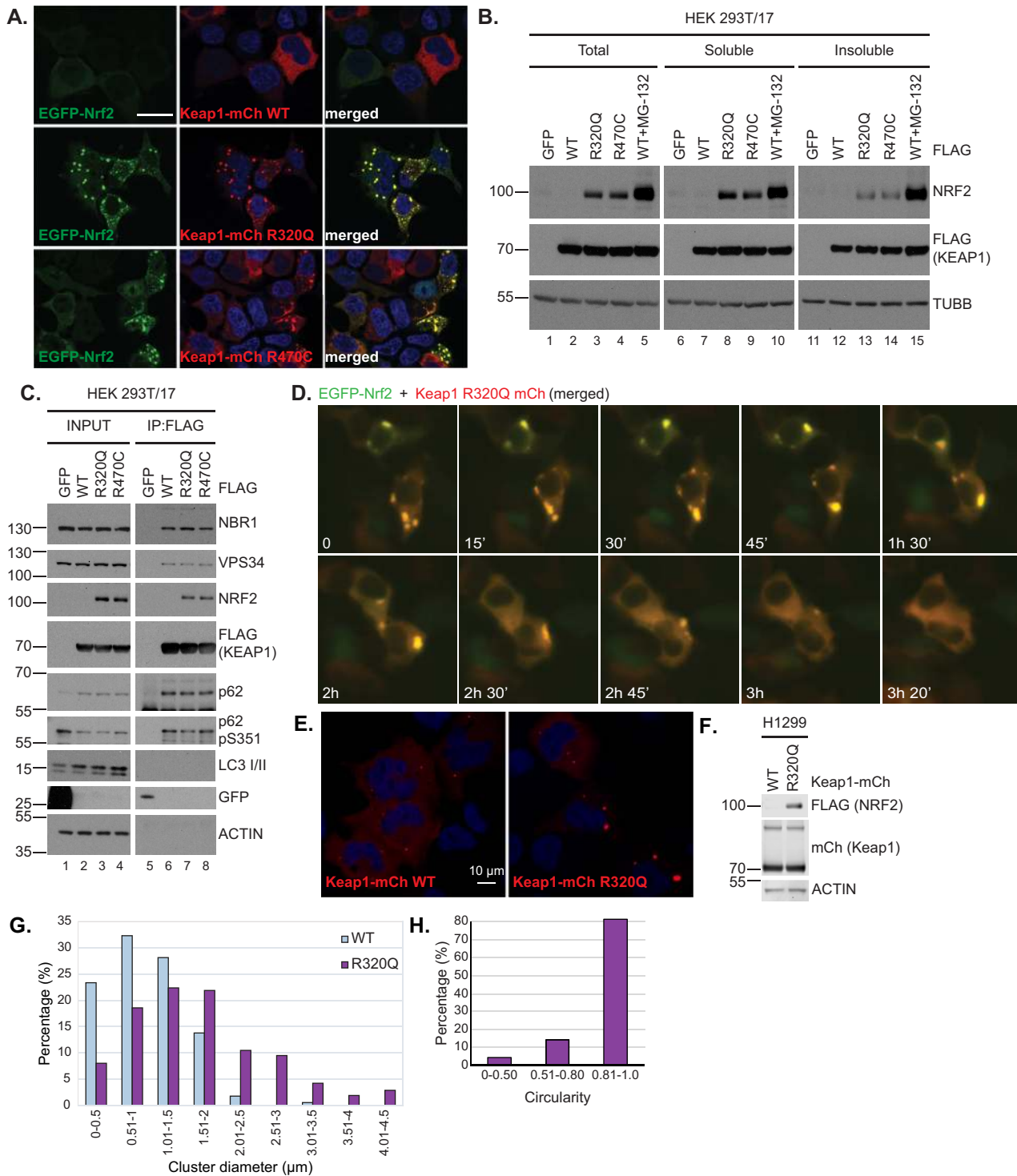


**FIG 6** KEAP1 ANCHOR mutants interact with proteins involved in autophagy and form circular, insoluble clusters. (A) HEK 293T/17 cells were transiently cotransfected with EGFP-Nrf2 (green) and Keap1-mCh WT, R320Q, or R470C. DAPI stain was used to visualize nuclei (blue). Scale bar = 20  $\mu$ m; confocal images are shown. (B) Triton X-100 solubility assay of HEK 293T/17 cells transiently transfected with the indicated FLAG-KEAP1 constructs. Sixteen hours posttransfection, cells were treated with DMSO or 10  $\mu$ M MG-132 for 8 h. Data are representative of those from a single experiment performed in biological triplicate. (C) IP/W.blot of HEK 293T/17 cells transfected with the indicated FLAG-KEAP1 constructs. FLAG-KEAP1 complexes were immunoprecipitated and probed for the indicated proteins. Data are representative of a single experiment performed in biological triplicate. (D) Time-lapse clearance of HEK 293T/17 cells cotransfected with EGFP-Nrf2 (green) and Keap1-R320Q mCh (red). Image acquisition was started 24 h posttransfection, and images were acquired every 4 min. Scale bar = 20  $\mu$ m. (E) H1299 cells were cotransfected with Keap1-mCh WT, R320Q, or R470C (red) and FLAG-NRF2 (not shown). Nuclei were stained with DAPI (blue). Scale bar = 10  $\mu$ m; confocal images are shown. (F) W.blot for indicated proteins of H1299 cells transiently transfected with mKeap1-mCh WT or R320Q constructs. Data are representative of those from a single experiment performed in biological triplicate. (G) Cluster diameter distribution in H1299 cells transiently expressing either Keap1-mCh WT (39 cells and 167 clusters analyzed) or R320Q (51 cells and 210 clusters analyzed). (H) Cluster circularity of Keap1-mCh R320Q-positive clusters (23 cells and 70 clusters analyzed).



interaction region (KIR) in p62 and is itself degraded by autophagy (100–103). We hypothesized that these clusters could represent autophagic flux of the KEAP1-NRF2 complexes with ANCHOR mutants. To evaluate KEAP1 association with components of the autophagy pathway, we performed IP/W.blot. Analysis of immunopurified complexes revealed that KEAP1 WT, R320Q, and R470C bound the autophagy cargo adaptors next to BRCA-1 (NBR1), p62, and an autophagy-specific form of p62 phosphorylated at serine 351 (pS351) (104–106) (Fig. 6C). Furthermore, KEAP1 WT, R320Q, and R470C bound VPS34, a class III phosphatidylinositol (PI) 3-kinase involved in the initial formation of the autophagosome (98, 99, 107) (Fig. 6C).

Upon formation of the autophagosome, p62 and NBR1 bind to and transport ubiquitylated substrates from the phagosome to the autophagosome, where the substrates are tethered to a lipidated form of light chain 3 (LC3) (98, 108). Lipidated LC3 can be detected via W.blot as a faster-migrating band, and conversion of LC3 I and II is routinely used as a marker of autophagic flux (96, 98, 108). KEAP1 WT, R320Q, and R470C were all deficient for binding with LC3 (Fig. 6C, lanes 6 to 8).

Overexpression of KEAP1 WT, R320Q, and R470C did not alter the total protein levels of NBR1 or VPS34; however, overexpression of KEAP1 WT, R320Q, and R470C resulted in increased p62 and LC3 I and II conversion levels and decreased levels of p62 pS351 (Fig. 6C, compare lane 1 with lanes 2 to 4). There were no appreciable differences in the effect of KEAP1 WT compared to the R320Q and R470C mutants with any of the autophagy proteins (Fig. 6C, compare lane 2 with lanes 3 and 4).

In order to visualize the formation of these complexes, mEGFP-Nrf2 and mKeap1-mCh R320Q were overexpressed in HEK 293T/17 cells for live-cell imaging studies. These movies revealed that the smaller punctate structures combined to form larger clusters that are ultimately cleared by the cell within a few hours (Fig. 6D; see also Movies S1 and S2). Moreover, accumulation of these aggregates was not cytotoxic, as several instances of cells proceeding through another round of division following aggregate clearance were observed (Movies S1 and S2). Notably, the clusters in the presence of R320Q were consistently larger (Fig. 6E to G). This difference in size was not due to differences in KEAP1 expression (Fig. 6F). Furthermore, a majority of the KEAP1-R320Q clusters exhibited a high degree of circularity, consistent with liquid-like properties characteristic of phase separation (Fig. 6H) (109, 110). To further confirm the morphology and subcellular architecture of the clusters, TEM coupled with correlative confocal imaging analysis was performed. TEM revealed KEAP1-R320Q clusters lacking a membrane, a defining characteristic of biomolecular condensates and membraneless organelles (Fig. 7A) (109, 110). Further TEM imaging analysis identified cocompartmentalization of KEAP1-R320Q and NRF2 biomolecular condensates with autophagic vesicles (AV) (Fig. 7B).

To identify the proteins contained in the biomolecular condensates, IF analysis of mKeap1-mCh and mEGFP-Nrf2 in H1299 cells was performed, and results confirmed that Keap1 and Nrf2 colocalize in the clusters (Fig. 8A). Moreover, IF analyses of FLAG-NRF2 and mKeap1-mCh R320Q revealed spherical clusters coated with endogenous polyubiquitin (polyUb), p62, and p62 pS351 (Fig. 8B). These clusters colocalized with overexpressed EGFP-LC3 but not with the following proteins: (i) proteasomal subunits (S20, PSMD2, or PSMD4) (Fig. S6), (ii) endogenous LC3, (iii) lysosomal marker LAMP2, or (iv) LysoTracker under basal conditions or following treatment with the autophagy inhibitor chloroquine (CQ) (Fig. S7A to C) (96, 97, 111). Furthermore, ATG5 siRNA depletion did not impact cluster formation or accumulation, suggesting that autophagy upstream of ATG5 is not involved (Fig. S7D and E). Knockdown of p62 via siRNA resulted in the absence of Keap1-NRF2 clusters (Fig. 8C; see also Fig. S7F). Taken together, these data support the p62-dependent formation of spherical membraneless organelles containing a KEAP1-positive core coated to various degrees with p62, p62 pS351, NRF2, and polyUb (Fig. 8D).

**KEAP1 ANCHOR mutants protect against chemotherapies that induce oxidative stress.** Prolonged NRF2 activation correlates with an increased resistance to chemotherapy and radiation treatment (22, 31–33, 36, 112–114). To determine the impact of

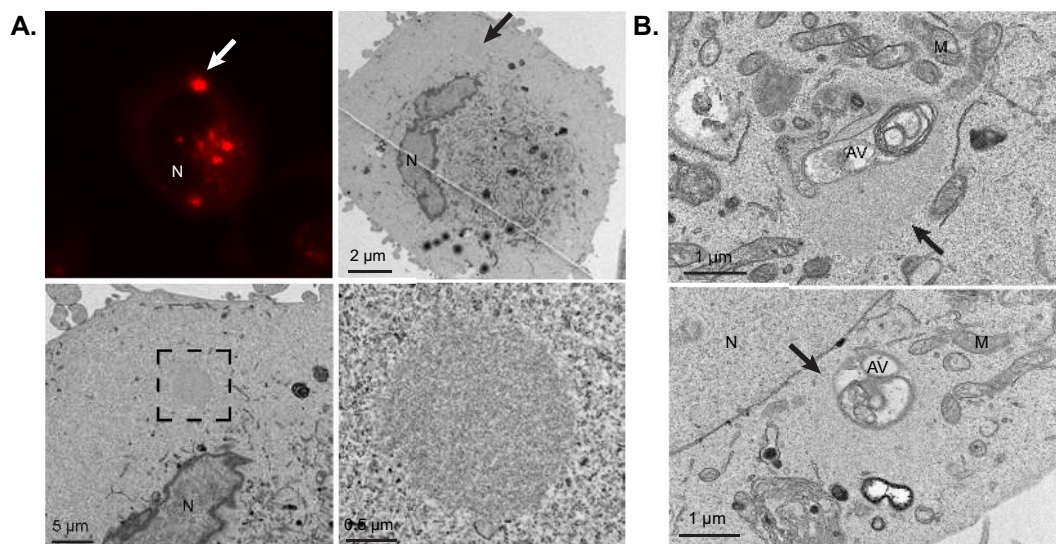


**FIG 7** Insoluble clusters formed by KEAP1 ANCHOR mutants are phase-separated biomolecular condensates. (A) Correlative epifluorescence and transmission electron microscopy (TEM) images of H1299 cells cotransfected with Keap1-mCh R320Q (red) and FLAG-NRF2 (not shown). Phase-separated biomolecular condensates are indicated by arrows or are boxed. N, nucleus. (B) TEM images as described for panel A from two different cells demonstrating cocompartmentalization of biomolecular condensates with autophagic vesicles (AV). M, mitochondria.

ANCHORs on cell viability, H1299 cells stably overexpressing mKeap1-mCh WT, R320Q, R470C, or mEGFP-Nrf2 were treated with bleomycin, which induces DNA damage via oxidative stress (115); cell viability and apoptosis were assayed by PrestoBlue and Caspase-Glo 3/7 assays, respectively (Fig. 9A; see also Fig. S8A). Analysis of 50% effective concentrations ( $EC_{50}$  values) for bleomycin demonstrated that KEAP1 R470C and R320Q exhibit significantly increased cell viability compared to KEAP1 WT (Fig. 9A) ( $P < 0.0001$ , unpaired  $t$  test). KEAP1 R320Q demonstrated a similar effect, though the increased  $EC_{50}$  value for the R320Q mutant compared to the WT was not statistically significant (Fig. 9A). To complement the cell viability data, levels of apoptotic induction were quantified using Caspase-Glo 3/7. The R470C mutant exhibited decreased activation of executioner caspases, which was significantly different from the case for the WT (Fig. 9B) ( $P = 0.0002$ , unpaired  $t$  test). KEAP1 R320Q also exhibited lower levels of activated caspases (Fig. 9B). Intriguingly, the protection conferred by the ANCHOR mutants was specific to bleomycin, as similar effects were not observed with either the DNA-damaging agent cisplatin or the microtubule destabilizer paclitaxel (Fig. S8B and C).

## DISCUSSION

Through biochemical and cell biology experimentation, we have defined five main attributes of the KEAP1 ANCHOR class. First, KEAP1 ANCHOR mutants occur at well-conserved and frequently mutated residues within KEAP1. Second, the KEAP1 ANCHOR phenotype is exclusive to NRF2; the abundance of other KEAP1-interacting proteins is unaffected. Third, KEAP1 ANCHOR mutants have a stabilizing effect on KEAP1 structure that decreases flexibility at key residues interfacing with NRF2; furthermore, mutation of the E493 residue identified from DMD simulation studies produces an ANCHOR phenotype. Fourth, the ANCHOR mutants form p62-dependent biomolecular condensates that are spherical and contain p62, p62 pS351, polyUb, and NRF2; these clusters are not delivered to the autophagy pathway for clearance and are formed by phase separation. Fifth, in the cell models tested, KEAP1 ANCHOR mutants show increased resistance to bleomycin treatment but not to cisplatin or paclitaxel.

Looking across all mutations reported in KEAP1, a strong correlation between mutational frequency and evolutionary conservation was observed. These findings parallel prior work demonstrating high mutational frequency in conserved residues

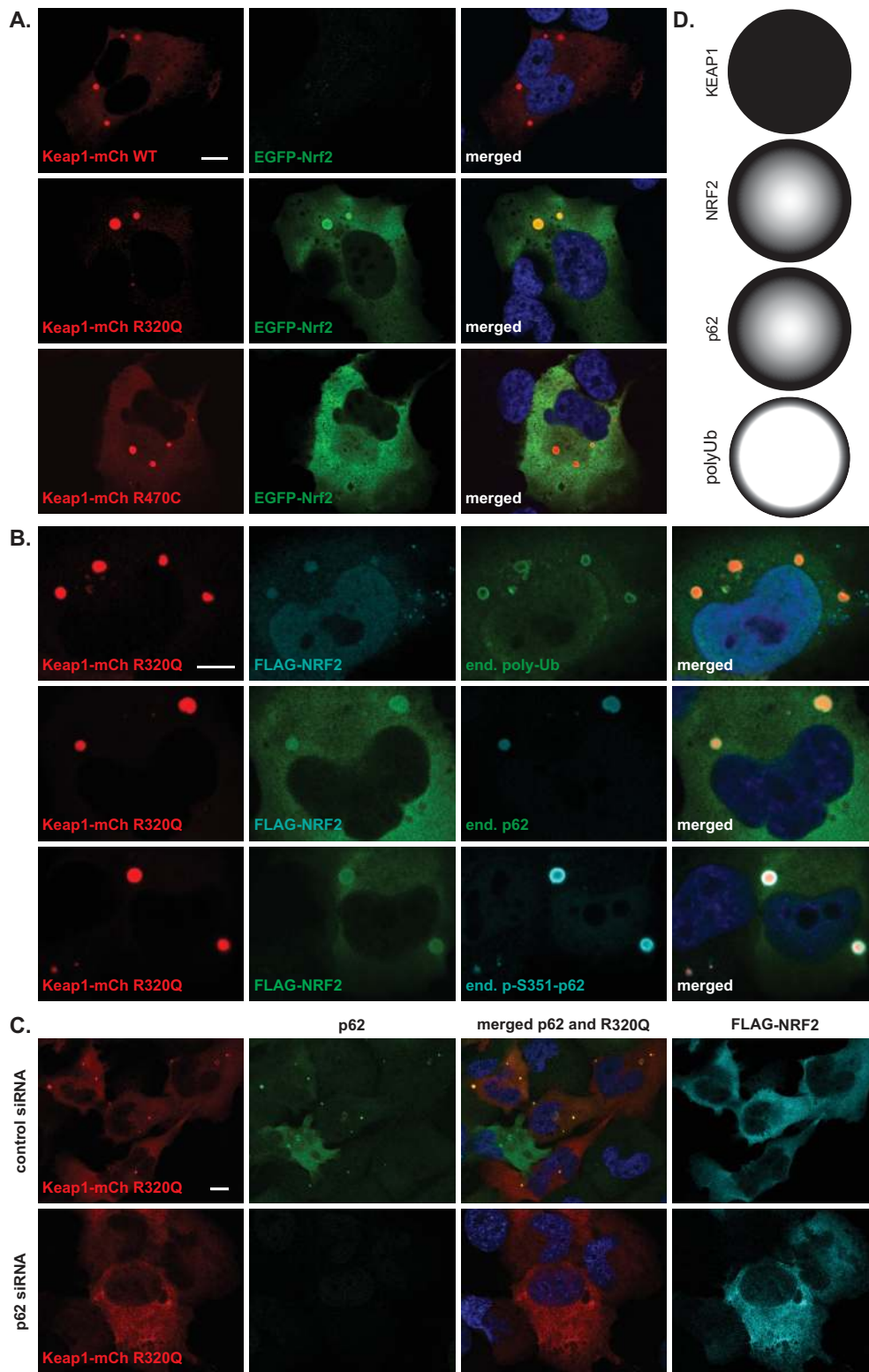


**FIG 8** KEAP1- and NRF2-positive clusters are positive for endogenous p62 and require p62 to form. (A) H1299 cells were cotransfected with Keap1-mCh WT, R320Q, or R470C (red) and EGFP-Nrf2 (green). Nuclei were stained with DAPI (blue). Scale bar = 10  $\mu$ m; confocal images are shown. (B) H1299 cells were cotransfected with Keap1-mCh R320Q (red) and FLAG-NRF2 (green or cyan) and stained for endogenous p62 and p62 pS351. Nuclei were stained with DAPI (blue). Scale bar = 10  $\mu$ m; confocal images are shown. (C) H1299 cells were transfected with either control or p62 siRNA, followed by cotransfection of Keap1-mCh R320Q (red) and FLAG-NRF2 (cyan). Transfected cells were stained for endogenous p62 (green). Scale bar = 20  $\mu$ m; confocal images are shown. Nuclei were stained with DAPI (blue). (D) Cartoon schematic of p62-dependent clusters containing KEAP1, NRF2, p62, and polyUb.

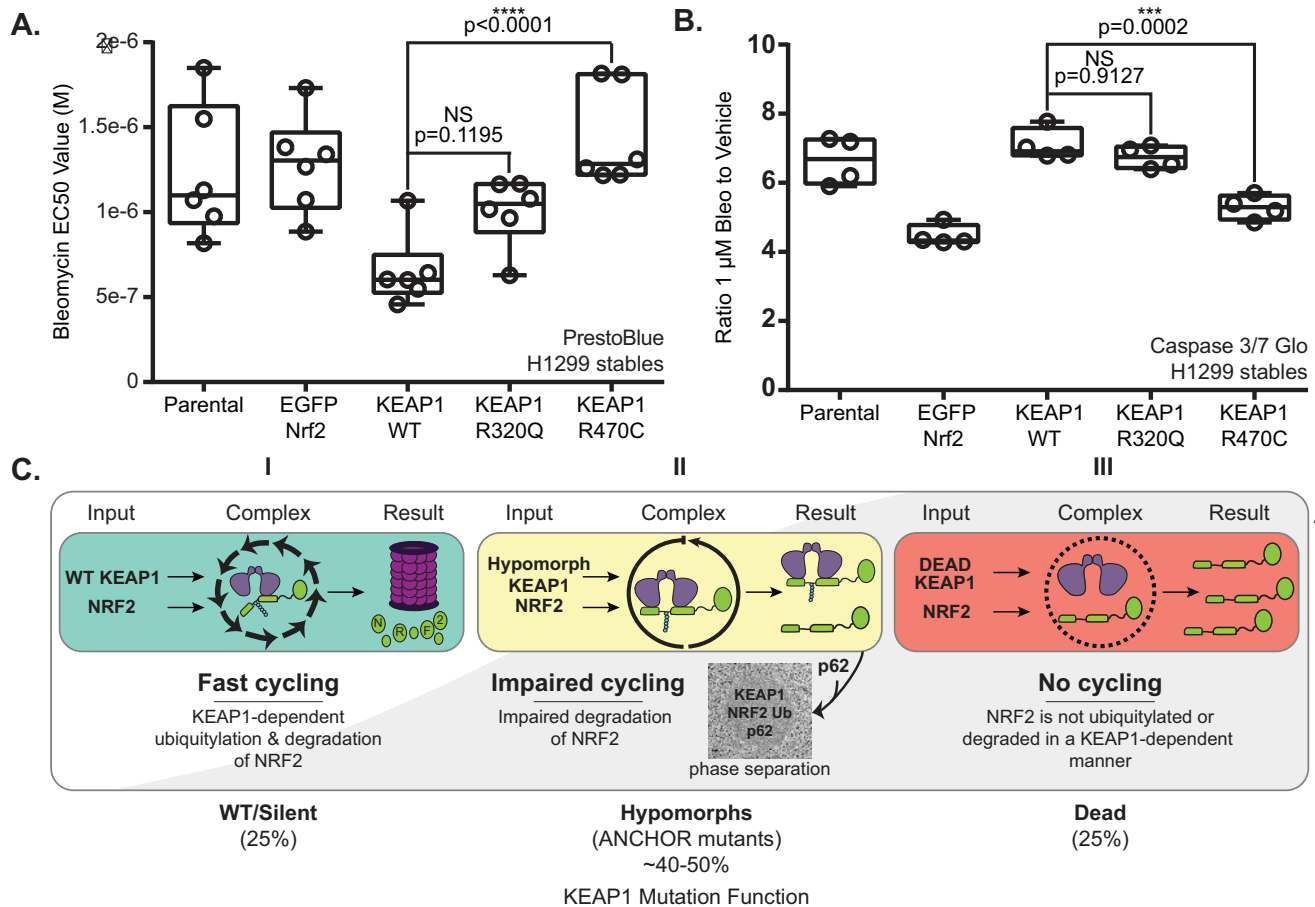


**FIG 9** Potential genotype-phenotype correlations of KEAP1 ANCHOR mutants. (A) EC<sub>50</sub> values of H1299 cells stably expressing indicated constructs and treated with bleomycin for 72 h. PrestoBlue measurements were plotted and fitted to determine EC<sub>50</sub> values. Each point represents the mean of technical quadruplicates performed in biological triplicate by two independent researchers. Error bars represent the SEMs. *P* values were determined using a one-way analysis of variance (ANOVA) with Tukey's multiple-comparison test. (B) H1299 cells stably expressing the indicated constructs were treated with 1 μM bleomycin for 72 h. Caspase-Glo 3/7 assay was used to measure levels of apoptosis. Each point represents the mean from a single experiment performed in technical quadruplicate. Error bars represent the SEMs. *P* values were determined using a one-way ANOVA with Tukey's multiple-comparison test. (C) Proposed model correlating KEAP1 cycling dynamics with NRF2 activity and KEAP1 mutation function. (I) Passenger or silent mutations are estimated to represent 25% of the mutations identified in LUSC. Functionally silent mutations result in low levels of nuclear NRF2 and maintain high rates of KEAP1 conformational cycling. (II) KEAP1 hypomorphs are estimated to represent 40 to 50% of LUSC mutations. We hypothesize that the ANCHOR mutations result in impaired or delayed cycling and form p62-dependent phase-separated biomolecular condensates that may represent intermediate aggregates between proteasomal and autophagic degradation. Consequently, KEAP1 hypomorphs exhibit elevated but not maximal levels of NRF2-dependent transcription. (III) Functionally dead mutations are unable to bind NRF2 and therefore do not cycle; consequently, NRF2 is neither ubiquitylated nor degraded in a KEAP1-dependent manner, resulting in maximal levels of nuclear NRF2 transcriptional activity and providing protection against DNA-damaging agents.

within TP53 (52). More specifically, the ANCHOR residues and known KEAP1-inactivating mutations, such as G333 and G480, are within the top 20 most conserved residues in KEAP1 (40, 44, 45, 116). We suggest that this approach can be used to prioritize mutations in other tumor suppressors and oncogenes for further study.

The unbiased BioID/MS approach and targeted interrogation of key protein-protein interactions suggest that with the exception of NRF2, the protein-protein interaction networks for ANCHOR mutants and wild-type KEAP1 are indistinguishable. We speculate that class I and class II ANCHOR mutants may differ in catalytic rates of NRF2 ubiquitylation or degradation; however, without structural insight into each of the mutations, this hypothesis remains speculative. We would have predicted that other DLG- and ETGE-containing substrates would also exhibit increased association with KEAP1 ANCHOR mutants. In fact, appreciable differences were not detected between ANCHOR mutants and NRF1, which contains both the DLG and ETGE motifs (66, 117). Of the substrates examined, only PGAM5 demonstrated stabilization in the presence of KEAP1 ANCHOR mutants; however, the ANCHOR mutants did not associate more with PGAM5 compared to WT KEAP1.



To date, the exact mechanism of how ubiquitylated NRF2 is delivered to the proteasome has not been described; however, we characterized novel KEAP1 interactions with the ubiquitin chaperone VCP and with two proteasomal ubiquitin receptors, PSMD2 and PSMD4. The KEAP1-VCP interaction merits further examination, as a recent report details the roles of VCP and ubiquitin cofactors UFD1/NPL4 and UBXN7 in removing ubiquitylated NRF2 from the KEAP1-CUL3 complex (27). In our studies, VCP depletion and inhibition had no effect on NRF2 protein levels in the presence of KEAP1 WT or R320Q, suggesting that VCP may not play a critical role in HEK 293T/17 or H1299 cells. The novel interactions between KEAP1 ANCHOR mutants and PSMD2 and PSMD4 indicate that ANCHOR mutants retain the ability to interact with the proteasome, which raises several possibilities for how the ANCHOR mutants may impair NRF2 degradation. First, ubiquitin removal and substrate unfolding of NRF2 may require additional ATP-dependent reactions or chaperone proteins that were not identified by the BioID approach. Second, the stabilized KEAP1 tertiary structure predicted by our simulation modeling and supported by the limited proteolysis and E493D mutation may preclude the removal of ubiquitin from NRF2 or the dissociation of the E3 complex after the ANCHOR attempts to present ubiquitylated NRF2 to the proteasome for degradation. Decreased flexibility at NRF2 contact points is a plausible explanation for the observed ANCHOR phenotype. It is possible that the R470C mutation disrupts salt bridge formation with amino acid residues D422 and/or E493, resulting in the observed stabilization. This mechanism of action is particularly attractive, as the KEAP1 D422N mutation also results in an ANCHOR phenotype (40). We provide data demonstrating that mutations to KEAP1 E493 result in an ANCHOR phenotype, as demonstrated by IP/W.blot and NRF2 transcriptional activity. These data provide further validation of the DMD simulation studies; additional DMD simulation studies may reveal biologically relevant mutations. Alterations to KEAP1 architecture and NRF2 contact residues support the hypothesis that ANCHOR mutants modify KEAP1 structure, resulting in impaired KEAP1 conformational cycling.

The identification of p62-dependent clusters was an unexpected phenotype observed with the ANCHOR mutants. These clusters are not specific to ANCHOR mutants, as they were also observed with KEAP1 WT in H1299 cells; however, ANCHOR mutations increased the accumulation of these clusters regardless of the cell type studied. Furthermore, NRF2 was detected in the biomolecular condensates only in the presence of KEAP1 ANCHOR mutants. The spherical shape of the clusters coupled with their live cell dynamics of fusion and dissipation along with the TEM imaging indicates membraneless phase separated organelles that have the capacity to compartmentalize with autophagic vesicles (109, 110, 118, 119). Identification of the stoichiometric ratios of these proteins within the cluster would help to determine the presence and composition of multimeric KEAP1-NRF2-p62 complexes. Biochemical isolation of the phase-separated clusters would also be informative for the identification of additional proteins as well as posttranslational modifications of proteins within the clusters. The exact nature of these clusters is intriguing given the unique shape and ordering of proteins within the clusters. Confocal imaging established that the clusters are circular and contain KEAP1 in the center, surrounded by rings of p62, p62 pS351, polyUb, and, in some instances, NRF2.

Given the dependence on p62 for cluster formation and the proximity to autophagic vesicles in TEM imaging, it is possible that these biomolecular condensates represent an intermediate between proteasomal and autophagic degradation pathways (106, 120–122). In fact, dynamic cross talk between proteasomal and autophagic degradation pathways is critical for cellular homeostasis, and proteotoxic stress has been shown to lead to increased autophagic flux (106, 120, 121). A recent report found that KEAP1/CUL3 ubiquitylates p62 on its ubiquitin-associated domain (UBA) and that this interaction is crucial for the recruitment of p62 into the autophagosome (123, 124). Furthermore, a role for p62 and polyubiquitin in the formation of phase-separated autophagic intermediates has been recently defined (125–127). Conformationally strained KEAP1 due to ANCHOR mutations may result in decreased or absent p62

ubiquitylation, preventing tethering to LC3 for autophagosome formation and maturation. We note that overexpression of LC3 is sufficient to target KEAP1-NRF2 clusters to autophagy; however, in the absence of LC3 overexpression, we found no evidence of autophagic engagement for KEAP1-NRF2 cluster clearance.

KEAP1 ANCHOR mutations are known to increase NRF2 transcriptional activity, which has been shown to be protective against chemotherapeutic insults (22, 31–33, 36, 112–114). Surprisingly, of the three cytotoxic drugs tested, KEAP1 ANCHOR mutations conferred protection only against bleomycin treatment, which induces DNA damage in cells through upregulating oxidative stress. This result was initially perplexing given the extensive body of literature demonstrating cytoprotective effects from elevated NRF2 transcriptional activity (22, 31–33, 36, 112–114); however, this finding raises several interesting points for discussion. First, mutations in KEAP1 result in a spectrum of phenotypes: functionally silent/WT, hypomorphic, and functionally dead (40). Approximately 25% of the KEAP1 LUSC mutations identified from the TCGA studies behaved comparably to KEAP1 WT (40). These silent mutations result in high levels of KEAP1 conformational cycling and low levels of nuclear NRF2 and NRF2 transcriptional activity (Fig. 9C, panel I). Hypomorphic mutations constitute 50% of KEAP1 LUSC mutations and include the ANCHOR mutations. These hypomorphic mutations result in impaired NRF2 degradation and may therefore impair KEAP1 cycling. Therefore, these mutations result in moderate levels of nuclear NRF2 and NRF2 transcriptional activity (Fig. 9C, panel II). Functionally dead mutations represent 25% of LUSC KEAP1 mutations. These KEAP1 mutants are unable to bind NRF2 and do not cycle; consequently, they exhibit elevated levels of both cytosolic and nuclear NRF2, with maximal NRF2 transcriptional activity (Fig. 9C, panel III). Second, genes that are transcriptionally upregulated in the presence of ANCHOR mutants may not be the same target genes as those upregulated in the presence of functionally dead mutations. Identification of these differentially expressed genes may provide further mechanistic understanding of ANCHOR mutations as well as reveal novel targets for clinical intervention.

In summary, through careful biochemical examination, we have defined novel interactions for KEAP1 with VCP, PSMD2, and PSMD4. Furthermore, we determined that KEAP1 ANCHOR mutations exclusively impact NRF2 association, appear to stabilize KEAP1 tertiary structure, and form p62-dependent phase-separated spherical clusters containing a KEAP1-positive core surrounded by unmodified and phosphorylated p62, polyUb, and NRF2. These studies reveal molecular insights into KEAP1 regulation and subcellular localization and suggest unique relationships between KEAP1 mutation, KEAP1 conformational cycling, and NRF2-driven transcription.

## MATERIALS AND METHODS

**Tissue culture and transfections.** HEK 293T/17 and NCI-H1299 (H1299) cells were obtained from the American Type Culture Collection (ATCC; Manassas, VA) and authenticated by the ATCC using short tandem repeat (STR) profiling. Cell lines were passaged for less than 3 months after resuscitation. *Keap1*<sup>-/-</sup> mouse embryonic fibroblasts (MEFs) were derived in collaboration with Luke Chen at North Carolina Central University and immortalized using simian virus 40 (SV40) large T antigen. HEK 293T/17 cells were grown in Dulbecco's modified Eagle medium (DMEM) supplemented with 10% fetal bovine serum (FBS). *Keap1*<sup>-/-</sup> MEFs were cultured in DMEM-F-12 supplemented with 10% FBS, 1% nonessential amino acids, and 1% sodium pyruvate. H1299 cells were grown in RPMI 1640 supplemented with 10% FBS. All cells were grown in a 37°C humidified incubator with 5% CO<sub>2</sub>. Expression constructs were transfected into HEK 293T/17 cells (7.50 × 10<sup>6</sup>/well in a 6-well format) with Lipofectamine 2000 (52887; Invitrogen, Carlsbad, CA) according to the manufacturer's protocols. H1299 cells (3.0 × 10<sup>6</sup>/well in a 6-well format) and *Keap1*<sup>-/-</sup> MEFs (1.5 × 10<sup>6</sup>/well in a 6-well format) were transfected with FuGENE HD (E231A; Promega, Madison, WI) in accordance with the manufacturer's protocols. Transfection of siRNAs in HEK 293T/17 cells (2.0 × 10<sup>6</sup> in a 6-well format) was performed with Lipofectamine RNAiMAX (Invitrogen; 56532) for 72 h unless otherwise stated.

**siRNA sequences.** Control (CNT) siRNA sequences are as follows: (i) 5' CGU ACG CGG AAU ACU UCG ACU UCG A 3' and (ii) 5' UCG AAG UAU UCC GCG UAC GCU AAG U 3'. siRNA sequences for *NFE2L2* are as follows: (i) 5' CCG GGA CAG AGT CAC CAT TTG ATT T 3', (ii) 5' CCC AGC AAT TCT ACC AGC CTC AAC T 3', and (iii) 5' GCT ATG TTG GAT GAG ATC AGC CTT A 3'. The siRNA sequences for *PGAM5* are as follows: (i) 5' ACG CGC GCC AUA GAG ACC ACC GAU A 3' and (ii) 5' CAC CUG CCA GGC GUC UGC AAA GUC A 3'. siRNA sequences for p62/*SQSTM1* are as follows: (i) 5' CAG AUG GAG UCG GAU AAC U 3', (ii) 5' CAG UCU CUG GCG GAG CAG A 3', and (iii) 5' GGC AGA AUC AGC UUC UGG U 3'. siRNA sequences for *VCP* are as follows: (i) 5' GGU AGA AGA GGA UGA UCC A 3', (ii) 5' CAG UUA CUA UGG AUG ACU U 3', and



(iii) 5' GGU AGA UAU UGG AAU UCC U 3'. siRNA sequences for *ATG5* are as follows: (i) 5' CAA CUU GUU UCA CGC UAU A [dT] [dT] 3' and (ii) 5' GAA CCA UAC UAU UUG CUU U [dT] [dT] 3'.

**Plasmids, expression vectors, and site-directed mutagenesis.** For all FLAG IP experiments, pcDNA3.1 containing FLAG-GFP was used as a negative control. pcDNA3.1 FLAG-KEAP1 WT, R320Q, and R470C as well as V51 pIRESpuro-GLUE (pGLUE) KEAP1 WT, R320Q, and R470C constructs were described previously (40). Entry clones for KEAP1 R320Q and R470C were generated using pcDNA 3.1 FLAG-KEAP1 R320Q and R470C constructs as described previously (40). Phusion high-fidelity DNA polymerase (M0530; New England BioLabs [NEB], Ipswich, MA) was used to generate the PCR product for the TOPO cloning reaction using the pCR8/GW/TOPO TA Cloning kit (200517; Thermo Fisher Scientific, Waltham, MA). TOPO cloning was performed according to the manufacturer's instructions. Cloning primers were as follows: forward, 5' ATG CAG CCA GAT CCC AGG 3', and reverse, 5' TCA ACA GGT ACA GTT CTG CTG GTC 3'. Resulting entry vectors were then gateway cloned into a custom gateway lentiviral vector, pHAGE-CMV-FLAG-BirA-DEST, to generate expression constructs for BirA<sup>\*</sup>-KEAP1 R320Q and R470C. Clones were sequence verified before use. pmCherry-N1 Keap1 WT (mKeap1-mCh WT) and pEGFP-C1-Nrf2 (mEGFP-Nrf2) were a kind gift from Albenka Dinkova-Kostova (University of Dundee, Dundee, United Kingdom) (15). mKeap1-mCh R320Q, mKeap1-mCh R470C, and pcDNA3.1 FLAG-KEAP1 E493D mutants were generated from PCR-based mutagenesis using the QuikChange XL site-directed mutagenesis kit (200517; Agilent, Santa Clara, CA) according to the manufacturer's instructions. Constructs were sequence verified before use; primer sequences for the mutagenesis are as follows: R320Q\_Forward, 5' CCA CTT TGG GCG CCT GGC AGG GCA CTG C 3'; R320Q\_Reverse, 5' GCA GTG CCC TGC CAG GCG CCC AAA GTG G 3'; R470C\_Forward, 5' CTG CAT ACA GCA AGC AGT TGA GCA CTG CCA C 3'; R470C\_Reverse, 5' GTG GCA GTG CTC AAC TGC TTG CTG TAT GCA G 3'; E493D\_Forward, 5' CAC TCG TTC CTG TCT GGG TAG TAA CAC TCA GC 3'; and E493D\_Reverse, 5' GCT GAG TGT TAC TAC CCA GAC AGG AAC GAG TG 3'.

**Live-cell imaging.** HEK 293T/17 cells were cotransfected with mEGFP-Nrf2 and mKeap1-mCh R320 and imaged the following day. Time-lapse phase-contrast and fluorescence images were acquired every 5 min for 10 h with an Olympus IX70 inverted fluorescence microscope enclosed within an environmental chamber controlled for temperature, relative humidity, and CO<sub>2</sub> and equipped with a 40×/0.6 Ph2 LCPlanFl objective lens and a Hamamatsu ORCA C4742-95 charge-coupled-device camera. Data acquisition was carried out with Velocity (version 5.5.1; PerkinElmer), and image processing was performed with ImageJ and Adobe Photoshop CS software.

IncuCyte live-cell imaging experiments were performed as reported previously, with minor modifications (128). HEK 293T/17 cells (1.50 × 10<sup>6</sup>/well in a 24-well format) were plated and transfected the next day with FLAG-KEAP1 WT, R320Q, or R470C (150 ng/well) along with mEGFP-Nrf2 or Venus-NRF2 (100 ng/well). Plates were immediately transferred into the IncuCyte ZOOM (Essen BioScience, Ann Arbor, MI) and housed inside a cell incubator at 37°C with 5% CO<sub>2</sub>. Images were taken every hour for 24 h with a 20× objective from four fields per well and from four technical replicates per condition in the phase and green channels (400-ms acquisition). Automated image processing on the fluorescence and phase channels was accomplished by applying an appropriate processing definition. Total green object integrated intensity (GCU × μm<sup>2</sup>/image) was normalized by cell confluence. Data presented represent the averages from three biological replicates and are reported as means ± standard errors of the means.

**Immunopurification and Western blotting.** For FLAG/mCherry immunopurification, HEK 293T/17 cells (7.5 × 10<sup>6</sup>/well in a 6-well format) or H1299 cells (3.0 × 10<sup>6</sup>/well in a 6-well format) were seeded and transfected and/or treated the following day for up to 24 h. Cells were washed with Dulbecco's phosphate-buffered saline (DPBS) and lysed in 255 μl (per well) of 0.1% NP-40 lysis buffer (0.1% NP-40, 10% glycerol, 50 mM HEPES [pH 8.0], 150 mM NaCl, and 2 mM EDTA) supplemented with Halt protease inhibitor Cocktail 100× (Thermo Scientific; 78429), Halt phosphatase inhibitor cocktail (100×; Thermo Scientific; 78426), and 10 mM *N*-ethylmaleimide (NEM) (Thermo Scientific; 23030). Cells were lysed on ice for 30 min, followed by a 30-min centrifugation at 16,000 × *g* at 4°C. Cleared lysates were quantified using the Pierce bicinchoninic acid (BCA) protein assay kit (Thermo Scientific; 23225) and incubated with an EZview red anti-FLAG M2 affinity gel (Sigma F2426; St. Louis, MO) or 1 μg of mCherry antibody (ab16745; Abcam, Cambridge, UK) prior to being washed 4 times with 0.1% NP-40 lysis buffer and eluted with 4× NuPAGE LDS sample buffer (NP0007; Life Technologies, Carlsbad, CA). For immunoprecipitation of mKeap1-mCh or mEGFP-Nrf2, cells were lysed and cleared as described above and precleared for 1 h with Pierce protein A/G-agarose (Thermo Scientific; 20421). Lysates were then incubated with mCherry antibody or GFP antibody (Abcam; ab290) overnight at 4°C. The following day, lysates were incubated for 1 h with Pierce protein A/G resin, followed by elution with NuPAGE LDS sample buffer as described above. For siRNA experiments, HEK 293T/17 cells were lysed in radioimmunoprecipitation assay (RIPA) buffer (1% NP-40, 0.1% SDS, 10% glycerol, 25 mM Tris-HCl [pH 7 to 8], 0.25% sodium deoxycholate, 150 mM NaCl, and 2 mM EDTA) supplemented with protease and phosphatase inhibitor cocktails and 10 mM NEM 72 h posttransfection.

**Antibodies used for W.blot analysis.** GFP (ab290), HMOX1 (ab13243), mCherry (ab16745), and PGAM5 (ab126534) antibodies were purchased from Abcam (Cambridge, UK). MCM3 (A300-192A), PALB2 (A301-246A), PSMD4 (A303-55A), p62/SQSTM1 A302-856A), and vesicular stomatitis virus glycoprotein (VSV-G) (A190-131A) antibodies were purchased from Bethyl Laboratories (Montgomery, TX). *ATG5* (2630), *BCL2* (2876B), *CUL3* (2759), *IKKB* (2684), K48 linkage-specific polyubiquitin clone D9D5 (8081), LC3A/B clone D3U4C XP (12741), *NBR1* clone D2E6 (9891), *NRF1* (8052), p62/SQSTM1 (8025), *VCP* (2648), and *VPS34* (4263) were purchased from Cell Signaling Technologies (Danvers, MA). *PSMD2* (PA5-27663) antibody was obtained from Invitrogen. The phosphorylated p62 (SQSTM1) (Ser351) p62/SQSTM1 (PM074) antibody was obtained from MBL International (Woburn, MA). KEAP1 (10503-2-AP) antibody was obtained from Proteintech (Rosemont, IL). Antihemagglutinin (anti-HA) high-affinity rat antibody (11 867

423 001) was purchased from Roche Diagnostics (Mannheim, Germany). NRF2-H300 (SC-13032) antibody was purchased from Santa Cruz Biotechnology (Dallas, TX). Actin (A5316), FLAG M2 (F1804), and beta tubulin (T7816) antibodies were purchased from Sigma. The following secondary antibodies were purchased from Jackson ImmunoResearch (West Grove, PA): peroxidase-conjugated IgG fraction monoclonal mouse anti-rabbit IgG, light chain specific (211-032-171), peroxidase-conjugated AffiniPure goat anti-mouse IgG, light chain specific (115-035-174), peroxidase-conjugated AffiniPure donkey anti-mouse IgG (H+L) (715-035-150), peroxidase-conjugated AffiniPure donkey anti-goat IgG (H+L) (705-035-003), peroxidase-conjugated AffiniPure donkey anti-rat IgG (H+L) (712-035-150), and peroxidase-conjugated AffiniPure donkey anti-rabbit IgG (H+L) (711-035-152). Secondary antibodies for LI-COR were purchased from LI-COR Biosciences (Lincoln, NE): IRDye 680LT goat anti-rabbit IgG (925-68021), IRDye 680LT goat anti-mouse IgG (925-68020), IRDye 800CW goat anti-mouse IgG (925-32210), and IRDye 800CW goat anti-rabbit IgG (925-32211).

**Antibodies used for IF analysis.** LAMP2 antibody (555803) was obtained from BD Biosciences (Franklin, NJ). The LC3B (2775) and LC3B D11 XP (3868) antibodies were obtained from Cell Signaling Technology. The polyubiquitinated conjugate clone FK1 antibody (BML-PW8805) and the proteasome 20S  $\alpha$  subunit antibody (BML-PW8265-0100; 1:150) were purchased from Enzo Life Sciences (Farmingdale, NY). PSMD2 antibody (PA5-27663; 1:200) was obtained from Invitrogen. PSMD4 antibody (A303-855A; 1:200) was obtained from Bethyl Laboratories. The following secondary antibodies were all purchased from Jackson ImmunoResearch Laboratories: fluorescein isothiocyanate (FITC)-AffiniPure donkey anti-mouse IgG (715-095-150), Alexa Fluor 647-AffiniPure donkey anti-rabbit IgG (711-605-152), Alexa Fluor 647-AffiniPure donkey anti-mouse IgG (715-505-150), and rhodamine red-X (RRX)-AffiniPure donkey anti-mouse IgG (715-295-150).

**Small-molecule reagents.** The following chemicals were purchased from Cayman Chemicals (Ann Arbor, MI): bleomycin sulfate (13877), cisplatin (13119), CB-5083 (19311), *N*<sup>2</sup>,*N*<sup>4</sup>-dibenzylquinazoline-2,4-diamine (DBEQ; 15318), and Eeyrestatin 1 (Eey1; 10012609). Cycloheximide (CHX; 1010083) was purchased from MP Biomedicals (Santa Ana, CA). The following chemicals were purchased from Sigma: chloroquine (CQ; C6628), L-sulforaphane (SFN; S6317), and *tert*-butylhydroquinone (tBHQ; 112941). Bardoxolone methyl (CDDO; S8078) was obtained from Selleck Chemicals (Houston, TX). Paclitaxel (TXD01) was obtained from Cytoskeleton, Inc. (Denver, CO). The following chemicals were purchased from Calbiochem (Darmstadt, Germany): MG-132 (474790) and MLN4924 (505477001).

**Immunostaining and confocal images.** Immunostaining and confocal imaging were performed as reported previously, with minor modifications (128). Briefly, HEK 293T/17 or H1299 cells were plated on coverslips coated with 10  $\mu$ g/ml of fibronectin in the appropriate culture media and allowed to attach overnight. For experiments that required exogenous expression of tagged proteins, transfection was performed 24 h postplating, and cells were stained the following day. Cells were fixed in 4% paraformaldehyde in cytoskeletal buffer [5 mM piperazine-*N,N'*-bis(2-ethanesulfonic acid) (PIPES; pH 6.0), 137 mM NaCl, 5 mM KCl, 1.1 mM Na<sub>2</sub>HPO<sub>4</sub>, 0.4 mM KH<sub>2</sub>PO<sub>4</sub>, 0.4 mM MgCl<sub>2</sub>, 0.4 mM NaHCO<sub>3</sub>, 2 mM EGTA, and 50 mM glucose] for 15 min and permeabilized with 0.1% Triton X-100 in phosphate-buffered saline (PBS) for 5 min. After blocking with 1% bovine serum albumin (BSA) in PBS, cells were incubated overnight with the primary antibodies and then incubated with the appropriate fluorescence-conjugated secondary antibodies for 1 h. The following primary antibodies were used: anti-FLAG (1:1,000; Sigma), anti-p62 (1:150; Cell Signaling Technology), anti-p-S351-p62 (1:300; MBL International), anti-LC3B (1:150; Cell Signaling Technology), anti-LAMP2 (1:150; BD Biosciences), and anti-polyubiquitinated conjugate FK1 (1:250; Enzo Life Sciences). The following secondary antibodies were used: FITC-anti-mouse IgG (1:300), Alexa Fluor 647-anti-rabbit IgG (1:500), Alexa Fluor 647-anti-mouse IgG (1:300), and RRX-anti-mouse IgG (1:2,000). 4',6-Diamidino-2-phenylindole (DAPI) staining was performed for nuclear detection. Coverslips were mounted to slides using the ProLong gold antifade mountant with DAPI (P36935; Thermo Fisher Scientific), and images were acquired using a Zeiss LSM 710 confocal laser-scanning microscope equipped with 40 $\times$ /1.3-numerical aperture (NA) Oil Plan Neo and 63 $\times$ /1.4-NA Oil Plan Apo objective lenses.

**Proximity ligation assays.** For detection of KEAP1 and NRF2 interactions, proximity ligation was performed with a Duolink II proximity ligation assay kit according to the protocol provided by the manufacturer (Sigma; DUO092101). Briefly, HEK 293T/17 cells stably expressing FLAG-KEAP1 (WT or mutants) were plated on fibronectin-coated coverslips, allowed to attach, fixed, and permeabilized as described above. For the PLA experiments with H1299 cells, transfections with the desired plasmids were performed 1 day after plating cells on coverslips. Cells were then incubated in blocking solution in a humidified chamber at 37°C for 30 min, followed by overnight coincubation with rabbit polyclonal antibodies against NRF2 (Santa Cruz; 1:200) and mouse monoclonal antibody against FLAG (Sigma; 1:1,000) in antibody diluent solution at 4°C. Cells were washed in buffer A and incubated with PLA probes (Sigma Duolink In Situ PLA Probe Anti-Rabbit PLUS [DUO92002] and Duolink In Situ PLA Probe Anti-Mouse MINUS [DUO92004] in antibody diluent (1:5 dilution) for 1 h at 37°C. They were then washed in buffer A and incubated with ligation solution (1:5 dilution of ligation buffer and 1:40 dilution of ligase in pure water) for 30 min at 37°C. After ligation, cells were washed in buffer A and subjected to amplification with detection reagents red (1:5 dilution of amplification stock and 1:80 dilution of polymerase in water) for 100 min at 37°C. Amplified samples were washed in buffer B, washed in buffer A, and counterstained for microtubules using antitubulin-FITC antibodies (Sigma; 1:500 dilution). The coverslips were mounted with Duolink II mounting medium with DAPI for nuclear detection. When analyzing PLA preparations in HEK 293T/17 cells, confocal Z-stack images of 10- $\mu$ m thickness were taken with a Z-step of 0.5  $\mu$ m (about 21 slices) at 512 by 512 pixels, using a Zeiss LSM710 spectral confocal laser-scanning microscope equipped with a 40/1.4 Oil Dic M27PlanApo objective lens. ImageJ software

was used to project all 21 slices per field into a two-dimensional (2D) image. When analyzing PLA preparations in H1299 cells, a single optical slice was captured per field from a depth of 4 to 5  $\mu\text{m}$  above the substrate to ensure that sampling was done from the same level for all preparations. Three channel images were taken for nine random fields per condition. Experiments were done in three biological replicates. The number of nuclei and PLA dots per image were quantified using BlobFinder software (129). The ratio of PLA dots to nuclei was set to 1 in FLAG-KEAP1 WT-expressing cells (untreated or dimethyl sulfoxide [DMSO] treated) and used to calculate PLA dot fold induction in cells expressing KEAP1 mutants or following treatment with NRF2 inducers.

**Correlative fluorescence and transmission electron microscopy.** Transfected H1299 cells were fixed with 4% paraformaldehyde, and an Olympus IX81 inverted light microscope was used to capture images in phase and red channels in order to map target regions to be examined at the ultrastructural level. Next, cells were fixed in 2.5% glutaraldehyde in 0.1 M sodium cacodylate buffer, postfixed in 1% buffered osmium tetroxide, dehydrated with a graded ethanol series, and embedded in Poly/Bed 812 epoxy resin (Polysciences, Inc., Warrington, PA). Ultrathin sections (80 nm) were cut, mounted on copper grids, and double stained with 4% uranyl acetate and Reynolds' lead citrate. Sections were observed using a JEOL JEM-1230 transmission electron microscope (JEOL USA Inc., Peabody, MA) operating at 80 kV. Digital images were taken using a Gatan Orius SC1000 CCD camera and Gatan Microscopy Suite v3.0 software (Gatan, Inc., Pleasanton, CA).

**Morphometric analysis of KEAP1-positive clusters.** For determination of KEAP1-positive cluster diameter, multiple images of H1299 cells transiently expressing mKeap1-mCh WT and R320Q were randomly captured using a confocal microscope as described above ("Immunostaining and confocal images"). The diameter of the mKeap1-mCh-positive clusters was measured using the red channel scaled images in the Zeiss ZEN 2011 (blue edition) software (Zeiss, Thornwood, NY).

For determination of the mKeap1-mCh-positive cluster circularity index, multiple images of mKeap1-mCh WT- and R320Q-expressing cells were randomly captured using an Olympus IX81 inverted light microscope. Binary images were generated in ImageJ by equally adjusting the threshold levels in red channel images. Circularity index values were obtained by using the ImageJ Analyze Particles plugin in which circularity is determined using the formula  $4\pi(\text{area}/\text{perimeter}^2)$ ; a perfect circle is defined as a circularity index of 1.0.

**KEAP1 ubiquitylation experiments.** Ubiquitylation of KEAP1 under denaturing conditions was performed with HEK 293T/17 cells transiently transfected with VSV-Ub1 or Venus-NPM1 and pGLUE-KEAP1 WT, R320Q, or R470C. Cells were lysed in preboiled SDS denaturing buffer (25 mM Tris, 150 mM NaCl, 1% SDS, and 1 mM EDTA) and boiled for 10 min. The cells were then diluted 1:5 in 0.5% NP-40 buffer (0.5% NP-40, 25 mM Tris-HCl [pH 7-8], and 150 mM NaCl) and normalized for protein content. A total of 250  $\mu\text{g}$  of protein was reserved for input, and 500  $\mu\text{g}$  of the lysate was immunoprecipitated with FLAG antibody for 2 h at 4°C. FLAG beads were washed 4 $\times$  with SDS denaturing buffer diluted 1:10 in 0.5% NP-40 lysis buffer. FLAG beads were then eluted with NuPAGE lysis buffer and boiled for 10 min at 70°C.

**BioID affinity purification and peptide generation.** HEK 293T/17 cells stably expressing BirA\*-KEAP1 WT, R320Q, or R470C were treated with 50  $\mu\text{M}$  biotin (Sigma; B4639) for 24 h. Cells were lysed in RIPA buffer supplemented with protease and phosphatase inhibitors, 10 mM NEM, and 1  $\mu\text{l}$  of Benzamide (Sigma E1404), cleared with ultracentrifugation, and protein normalized. Five milligrams of protein was used for streptavidin affinity purification (AP). Streptavidin-Sepharose high-performance beads (GE Healthcare 17-5113-01, Uppsala, Sweden) were washed three times in RIPA buffer prior to AP overnight at 4°C with nutation. Beads were washed once with RIPA buffer, twice with TAP lysis buffer (10% glycerol, 50 mM HEPES [pH 8.0], 150 mM NaCl, 2 mM EDTA, and 0.1% NP-40), and three times with 50 mM ammonium bicarbonate (pH 8.0). The precipitated proteins were trypsinized with 1  $\mu\text{g}$  of trypsin (Promega; V5111) for 16 h, followed by another 0.5  $\mu\text{g}$  of trypsin for 2 h. Trypsinization was performed directly on beads using a modified filter-aided sample preparation (FASP) protocol followed by desalting via a Pierce C<sub>18</sub> spin column (Thermo; 89870) and ethyl acetate cleanup.

**Mass spectrometry, data filtering, and bioinformatics.** Reverse-phase nano-high-performance liquid chromatography (nano-HPLC) coupled with a nanoACQUITY ultraperformance liquid chromatography (UPLC) system (Waters Corporation, Milford, MA) was used to separate trypsinized peptides. Trapping and separation of peptides were performed in a 2-cm column (Pepmap 100; 3- $\mu\text{m}$  particle size and 100-Å pore size), and a 25-cm EASYspray analytical column (75- $\mu\text{m}$  inside diameter [i.d.], 2.0- $\mu\text{m}$  C<sub>18</sub> particle size, and 100-Å pore size) at 300 nl/min and 35°C, respectively. Analysis of a 180-min gradient of 2 to 25% buffer B (0.1% formic acid in acetonitrile) was performed on an Orbitrap Elite mass spectrometer (Thermo Scientific). Data acquisition and ion source settings were previously published (65).

All raw mass spectrometry data were searched using MaxQuant version 1.5.2.6 (130, 131). Search parameters were as follows: UniProtKB/Swiss-Prot human canonical sequence database (downloaded 23 July 2013), static carbamidomethyl cysteine modification, specific trypsin digestion with up to two missed cleavages, variable protein N-terminal acetylation and methionine oxidation, match between runs, and label-free quantification (LFQ) with a minimum ratio count of 2 (132). Searched files were analyzed using Perseus version 1.5.1.6 for data filtering and visualization (133). Protein identifications were filtered to a 1% false-discovery rate (FDR), and potential contaminants and decoys were removed. LFQ intensities were  $\log_2$  transformed and filtered on proteins present in three replicates of at least one group. Missing values were imputed from a normal distribution using a downshift of 1.8 and a distribution width of 0.4. For volcano plots illustrating BioID/MS data, *P* values were determined using a two-tailed *t* test, and the FDR was calculated using the permutation test implemented in Perseus. The

mass spectrometry proteomics data have been deposited to the ProteomeXchange Consortium via the PRIDE partner repository with the data set identifier PXD008411 (134).

**Sequence variability for NRF2 and KEAP1.** The protein BLAST server was used to find 500 unique sequences for each gene and to analyze the sequence conservation for human NRF2 (UniProt accession number [Q16236](#)) and KEAP1 (UniProt accession number [Q14145](#)) (132, 135). All of the identified genes had at least 45% amino acid identity to the query sequence. The PROMALS3D webserver was used to create a multisequence alignment; default settings were used (136). Shannon entropy was calculated for the multiple sequence alignments using the Protein Variability Server with the default settings (50).

**DMD simulation data.** Five replicate DMD simulations of one million steps each for both KEAP1 WT and R470C were performed in the presence of the NRF2 peptide (87–90).

**Limited proteolysis.** *Keap1*<sup>-/-</sup> MEFs were seeded in 6-well plates and allowed to adhere overnight. The following day, cells were transfected with FLAG-KEAP1 constructs using FuGene HD according to the manufacturer's protocol. Twenty-four hours posttransfection, cells were washed twice with PBS and harvested in PBSt (0.1% Triton X-100 in PBS). Cells were snap-frozen in liquid nitrogen, thawed, and lysed for 1 h at 4°C. Lysates were cleared at 16,000 × *g* for 10 min at 4°C and protein normalized. Lysates were diluted to 1 mg/ml, and 75- $\mu$ l aliquots were taken. Twenty-five-microliter volumes of trypsin (Sigma; T1426) at the desired concentrations were added to lysates, and limited proteolysis was allowed to proceed for 15 min on ice. Reactions were quenched with 100  $\mu$ l of complete protease inhibitor and 100  $\mu$ M phenylmethylsulfonyl fluoride (PMSF). Samples were diluted with 4× LDS sample buffer and dithiothreitol (DTT) prior to boiling at 70°C for 10 min.

**hQR41-ARE luciferase assays.** The pGL2-hQR41-ARE luciferase assay construct was a kind gift from Jeffrey Johnson (92). The pRL-TK *Renilla* luciferase construct served as a control for transfection efficiency and cell viability (Promega; E2241). HEK 239T/17 cells were seeded in a 48-well format and cultured until 70% confluent. Cells were transfected with pGL2-hQR41-ARE luciferase (40 ng), pRL-TK (10 ng), cGLUE-NRF2 (10 ng), and FLAG-KEAP1 WT, R320Q, R470C, or E493D (100 ng) using Lipofectamine 2000 in accordance with the manufacturer's instructions. Twenty-four hours posttransfection, cells were lysed in 50  $\mu$ l of 1× passive lysis buffer (PLB) (Promega; E1941) for 15 min at room temperature. Firefly luciferase and *Renilla* luciferase were quantified using a dual-luciferase reporter assay system (Promega; E1960). Briefly, 10  $\mu$ l of cell lysate was transferred to a 96-well plate (PerkinElmer; 6005030) to which 10  $\mu$ l of luciferase assay reagent II (LAR II) was added, followed by luciferase measurement on a PerkinElmer EnSpire plate reader (PerkinElmer, Waltham, MA). Next, to quench the reaction and quantify *Renilla* luciferase, 10  $\mu$ l of Stop and Glo reagent was added and *Renilla* luciferase activity was measured. For all experiments, the ratio of hQR41-ARE firefly luciferase (FF) to *Renilla* luciferase for each well was determined. All experiments were performed with six technical replicates across five biological experiments conducted by two independent researchers. Resulting data were plotted and analyzed using Microsoft Excel.

**Triton X-100 solubility assays.** Harvested cell pellets were lysed for 1 h at 4°C in 1% Triton X-100 lysis buffer (1% Triton X-100, 10% glycerol, 25 mM Tris-HCl [pH 7 to 8], 150 mM NaCl, 2 mM EDTA) containing 10  $\mu$ l of RQ1 DNase (Promega; M6101). Forty-five microliters of lysate was removed for "total" sample, and the remaining lysate was subjected to centrifugation at 20,000 × *g* for 15 min at 4°C. Supernatant was removed, and 45  $\mu$ l was reserved for the soluble fraction, to which was added 20  $\mu$ l of 4× LDS sample buffer with 10 mM DTT. The insoluble fraction was dissolved in 200  $\mu$ l of 1× SDS sample buffer with DTT. Samples were sonicated with two 10-s pulses at 10% intensity using a Branson Ultrasonics sonifier (Branson S-450; Thermo Scientific) prior to SDS-PAGE.

**Cell viability assays.** H1299 cells (3.5 × 10<sup>3</sup>/well in a 96-well format) were seeded and allowed to adhere overnight. Serial drug dilutions were prepared, and cells were treated for 72 h. PrestoBlue cell viability reagent (Life Technologies Corporation; A13262) was added to wells according to the manufacturer's protocol. Measurements of resazurin conversion as a surrogate for mitochondrial respiration were taken by fluorescence on a PerkinElmer EnSpire plate reader (PerkinElmer). All experiments were performed in technical quadruplicate and biological triplicate by two independent researchers. Resulting data were plotted and analyzed using GraphPad Prism software version 7.0.

## SUPPLEMENTAL MATERIAL

Supplemental material for this article may be found at <https://doi.org/10.1128/MCB.00644-17>.

**SUPPLEMENTAL FILE 1**, PDF file, 8.9 MB.

**SUPPLEMENTAL FILE 2**, XLSX file, 0.1 MB.

**SUPPLEMENTAL FILE 3**, XLSX file, 0.1 MB.

**SUPPLEMENTAL FILE 4**, XLSX file, 0.1 MB.

**SUPPLEMENTAL FILE 5**, XLSX file, 0.1 MB.

**SUPPLEMENTAL FILE 6**, XLSX file, 0.1 MB.

**SUPPLEMENTAL FILE 7**, XLSX file, 0.1 MB.

**SUPPLEMENTAL FILE 8**, AVI file, 0.6 MB.

**SUPPLEMENTAL FILE 9**, AVI file, 0.4 MB.



## ACKNOWLEDGMENTS

This work was supported by the following: funds from the American Cancer Society (RSG-14-068-01-TBE), NIH/NCI RO1 (RO1-CA216051), and NIH/NCI U54 (U54-CA156733) to M.B.M. and from Cancer Cell Biology Training Program T32 (CA071341-16) and NC TraCS TL1 Predoctoral Training Program T32 (5TL1TR001110-02) to E.W.C. N.V.D. also acknowledges support from NIH grants R01-GM114015, R01-GM064803, and R01-GM123247. S.J.W. acknowledges support from NIH/CNI U54 (U54-CA156735). TEM sample preparation and image analyses were carried out by the Microscopy Services Laboratory, UNC Pathology and Laboratory Medicine, supported in part by P30 CA016086 Cancer Center Core Support Grant to the UNC Lineberger Comprehensive Cancer Center.

We kindly thank the members of the Major laboratory for support, feedback, reagents, and expertise regarding experimental design and procedures.

We declare that no conflicts of interest exist.

Author contributions were as follows: conceptualization, E.W.C. and M.B.M.; experimental design, E.W.C., P.F.S., E.M.C., D.G., and M.B.M.; Shannon entropy analysis, J.S.H.; cell imaging studies, P.F.S.; mass spectrometry studies, E.W.C. and D.G.; data analysis, E.W.C., D.G., P.F.S., and M.B.M.; DMD simulation studies, D.D.M. and N.V.D.; hQR41-ARE luciferase assays, E.W.C. and S.J.W.; TEM studies, P.F.S.; writing/editing, E.W.C., E.M.C., and M.B.M.; supervision, M.B.M.; and funding support, E.W.C. and M.B.M.

## REFERENCES

- Howlander N, Noone AM, Krapcho M, Miller D, Bishop K, Kosary CL, Yu M, Ruhl J, Tatalovich Z, Mariotto A, Lewis DR, Chen HS, Feuer EJ, Cronin KA (ed) April 2017. SEER cancer statistics review, 1975–2014. Based on November 2016 SEER data submission, National Cancer Institute, Bethesda, MD. [https://seer.cancer.gov/csr/1975\\_2014/](https://seer.cancer.gov/csr/1975_2014/).
- Herbst RS, Heymach JV, Lippman SM. 2008. Lung cancer. *N Engl J Med* 359:1367–1380. <https://doi.org/10.1056/NEJMra0802714>.
- Alberg AJ, Ford JG, Samet JM, American College of Chest Physicians. 2007. Epidemiology of lung cancer: ACCP evidence-based clinical practice guidelines (2nd edition). *Chest*. 132:295–555. <https://doi.org/10.1378/chest.07-1347>.
- Ries LAG YJ, Keel GE, Eisner MP, Lin YD, Horner M-J (ed). 2007. Cancer of the lung, 1988–2001, patient and tumor characteristics. *In* SEER survival monograph: cancer survival among adults: U.S. SEER Program. NIH publication number 07-6215. National Cancer Institute, Bethesda, MD.
- Cancer Genome Atlas Research Network. 2012. Comprehensive genomic characterization of squamous cell lung cancers. *Nature* 489: 519–525. <https://doi.org/10.1038/nature11404>.
- Itoh K, Mimura J, Yamamoto M. 2010. Discovery of the negative regulator of Nrf2, Keap1: a historical overview. *Antioxid Redox Signal* 13: 1665–1678. <https://doi.org/10.1089/ars.2010.3222>.
- Cullinan SB, Gordan JD, Jin J, Harper JW, Diehl JA. 2004. The Keap1-BTB protein is an adaptor that bridges Nrf2 to a Cul3-based E3 ligase: oxidative stress sensing by a Cul3-Keap1 ligase. *Mol Cell Biol* 24: 8477–8486. <https://doi.org/10.1128/MCB.24.19.8477-8486.2004>.
- Furukawa M, Xiong Y. 2005. BTB protein Keap1 targets antioxidant transcription factor Nrf2 for ubiquitination by the Cullin 3-Roc1 ligase. *Mol Cell Biol* 25:162–171. <https://doi.org/10.1128/MCB.25.1.162-171.2005>.
- Zhang DD, Lo SC, Cross JV, Templeton DJ, Hannink M. 2004. Keap1 is a redox-regulated substrate adaptor protein for a Cul3-dependent ubiquitin ligase complex. *Mol Cell Biol* 24:10941–10953. <https://doi.org/10.1128/MCB.24.24.10941-10953.2004>.
- Kobayashi A, Kang MI, Okawa H, Ohtsuiji M, Zenke Y, Chiba T, Igarashi K, Yamamoto M. 2004. Oxidative stress sensor Keap1 functions as an adaptor for Cul3-based E3 ligase to regulate proteasomal degradation of Nrf2. *Mol Cell Biol* 24:7130–7139. <https://doi.org/10.1128/MCB.24.16.7130-7139.2004>.
- Taguchi K, Motohashi H, Yamamoto M. 2011. Molecular mechanisms of the Keap1-Nrf2 pathway in stress response and cancer evolution. *Genes Cells* 16:123–140. <https://doi.org/10.1111/j.1365-2443.2010.01473.x>.
- Lo SC, Li X, Henzl MT, Beamer LJ, Hannink M. 2006. Structure of the Keap1:Nrf2 interface provides mechanistic insight into Nrf2 signaling. *EMBO J* 25:3605–3617. <https://doi.org/10.1038/sj.emboj.7601243>.
- Tong KI, Kobayashi A, Katsuoka F, Yamamoto M. 2006. Two-site substrate recognition model for the Keap1-Nrf2 system: a hinge and latch mechanism. *Biol Chem* 387:1311–1320. <https://doi.org/10.1515/BC.2006.164>.
- Tong KI, Katoh Y, Kusunoki H, Itoh K, Tanaka T, Yamamoto M. 2006. Keap1 recruits Neh2 through binding to ETGE and DLG motifs: characterization of the two-site molecular recognition model. *Mol Cell Biol* 26:2887–2900. <https://doi.org/10.1128/MCB.26.8.2887-2900.2006>.
- Baird L, Lleres D, Swift S, Dinkova-Kostova AT. 2013. Regulatory flexibility in the Nrf2-mediated stress response is conferred by conformational cycling of the Keap1-Nrf2 protein complex. *Proc Natl Acad Sci U S A* 110:15259–15264. <https://doi.org/10.1073/pnas.1305687110>.
- Kensler TW, Wakabayashi N, Biswal S. 2007. Cell survival responses to environmental stresses via the Keap1-Nrf2-ARE pathway. *Annu Rev Pharmacol Toxicol* 47:89–116. <https://doi.org/10.1146/annurev.pharmtox.46.120604.141046>.
- Ogura T, Tong KI, Mio K, Maruyama Y, Kurokawa H, Sato C, Yamamoto M. 2010. Keap1 is a forked-stem dimer structure with two large spheres enclosing the intervening, double glycine repeat, and C-terminal domains. *Proc Natl Acad Sci U S A*. 107:2842–2847. <https://doi.org/10.1073/pnas.0914036107>.
- Watai Y, Kobayashi A, Nagase H, Mizukami M, McEvoy J, Singer JD, Itoh K, Yamamoto M. 2007. Subcellular localization and cytoplasmic complex status of endogenous Keap1. *Genes Cells* 12:1163–1178. <https://doi.org/10.1111/j.1365-2443.2007.01118.x>.
- Zhang DD, Hannink M. 2003. Distinct cysteine residues in Keap1 are required for Keap1-dependent ubiquitination of Nrf2 and for stabilization of Nrf2 by chemopreventive agents and oxidative stress. *Mol Cell Biol* 23:8137–8151. <https://doi.org/10.1128/MCB.23.22.8137-8151.2003>.
- Nguyen T, Sherratt PJ, Huang HC, Yang CS, Pickett CB. 2003. Increased protein stability as a mechanism that enhances Nrf2-mediated transcriptional activation of the antioxidant response element. Degradation of Nrf2 by the 26 S proteasome. *J Biol Chem* 278:4536–4541.
- McMahon M, Itoh K, Yamamoto M, Hayes JD. 2003. Keap1-dependent proteasomal degradation of transcription factor Nrf2 contributes to the negative regulation of antioxidant response element-driven gene expression. *J Biol Chem* 278:21592–21600. <https://doi.org/10.1074/jbc.M300931200>.
- Taguchi K, Yamamoto M. 2017. The KEAP1-NRF2 system in cancer. *Front Oncol* 7:85. <https://doi.org/10.3389/fonc.2017.00085>.

23. Iso T, Suzuki T, Baird L, Yamamoto M. 2016. Absolute amounts and status of the Nrf2-Keap1-Cul3 complex within cells. *Mol Cell Biol* 36:3100–3112. <https://doi.org/10.1128/MCB.00389-16>.
24. Baird L, Dinkova-Kostova AT. 2013. Diffusion dynamics of the Keap1-Cullin3 interaction in single live cells. *Biochem Biophys Res Commun* 433:58–65. <https://doi.org/10.1016/j.bbrc.2013.02.065>.
25. Baird L, Swift S, Lleres D, Dinkova-Kostova AT. 2014. Monitoring Keap1-Nrf2 interactions in single live cells. *Biotechnol Adv* 32:1133–1144. <https://doi.org/10.1016/j.biotechadv.2014.03.004>.
26. Baird L, Dinkova-Kostova AT. 2011. The cytoprotective role of the Keap1-Nrf2 pathway. *Arch Toxicol* 85:241–272. <https://doi.org/10.1007/s00204-011-0674-5>.
27. Tao S, Liu P, Luo G, Rojo de la Vega M, Chen H, Wu T, Tillotson J, Chapman E, Zhang DD. 2017. p97 negatively regulates NRF2 by extracting ubiquitylated NRF2 from the KEAP1-CUL3 E3 complex. *Mol Cell Biol* 37:e00660-16. <https://doi.org/10.1128/MCB.00660-16>.
28. Kobayashi M, Yamamoto M. 2006. Nrf2-Keap1 regulation of cellular defense mechanisms against electrophiles and reactive oxygen species. *Adv Enzyme Regul* 46:113–140. <https://doi.org/10.1016/j.advrenreg.2006.01.007>.
29. Singh A, Misra V, Thimmulappa RK, Lee H, Ames S, Hoque MO, Herman JG, Baylín SB, Sidransky D, Gabrielson E, Brock MV, Biswal S. 2006. Dysfunctional KEAP1-NRF2 interaction in non-small-cell lung cancer. *PLoS Med* 3:e420. <https://doi.org/10.1371/journal.pmed.0030420>.
30. Sykietis GP, Bohmann D. 2010. Stress-activated cap'n'collar transcription factors in aging and human disease. *Sci Signal* 3:re3. <https://doi.org/10.1126/scisignal.3112re3>.
31. Solis LM, Behrens C, Dong W, Suraokar M, Ozburn NC, Moran CA, Corvalán AH, Biswal S, Swisher SG, Bekele BN, Minna JD, Stewart DJ, Wistuba II. 2010. Nrf2 and Keap1 abnormalities in non-small cell lung carcinoma and association with clinicopathologic features. *Clin Cancer Res* 16:3743–3753. <https://doi.org/10.1158/1078-0432.CCR-09-3352>.
32. Wang XJ, Sun Z, Villeneuve NF, Zhang S, Zhao F, Li Y, Chen W, Yi X, Zheng W, Wondrak GT, Wong PK, Zhang DD. 2008. Nrf2 enhances resistance of cancer cells to chemotherapeutic drugs, the dark side of Nrf2. *Carcinogenesis* 29:1235–1243. <https://doi.org/10.1093/carcin/bgn095>.
33. Ohta T, Iijima K, Miyamoto M, Nakahara I, Tanaka H, Ohtsuiji M, Suzuki T, Kobayashi A, Yokota J, Sakiyama T, Shibata T, Yamamoto M, Hirohashi S. 2008. Loss of Keap1 function activates Nrf2 and provides advantages for lung cancer cell growth. *Cancer Res* 68:1303–1309. <https://doi.org/10.1158/0008-5472.CAN-07-5003>.
34. Satoh H, Moriguchi T, Takai J, Ebina M, Yamamoto M. 2013. Nrf2 prevents initiation but accelerates progression through the Kras signaling pathway during lung carcinogenesis. *Cancer Res* 73:4158–4168. <https://doi.org/10.1158/0008-5472.CAN-12-4499>.
35. Lau A, Villeneuve NF, Sun Z, Wong PK, Zhang DD. 2008. Dual roles of Nrf2 in cancer. *Pharmacol Res* 58:262–270. <https://doi.org/10.1016/j.phrs.2008.09.003>.
36. Homma S, Ishii Y, Morishima Y, Yamadori T, Matsuno Y, Haraguchi N, Kikuchi N, Satoh H, Sakamoto T, Hizawa N, Itoh K, Yamamoto M. 2009. Nrf2 enhances cell proliferation and resistance to anticancer drugs in human lung cancer. *Clin Cancer Res* 15:3423–3432. <https://doi.org/10.1158/1078-0432.CCR-08-2822>.
37. Zhang DD. 2010. The Nrf2-Keap1-ARE signaling pathway: the regulation and dual function of Nrf2 in cancer. *Antioxid Redox Signal* 13:1623–1626. <https://doi.org/10.1089/ars.2010.3301>.
38. Gao J, Aksoy BA, Dogrusoz U, Dresdner G, Gross B, Sumer SO, Sun Y, Jacobsen A, Sinha R, Larsson E, Cerami E, Sander C, Schultz N. 2013. Integrative analysis of complex cancer genomics and clinical profiles using the cBioPortal. *Sci Signal* 6:p11. <https://doi.org/10.1126/scisignal.2004088>.
39. Cerami E, Gao J, Dogrusoz U, Gross BE, Sumer SO, Aksoy BA, Jacobsen A, Byrne CJ, Heuer ML, Larsson E, Antipin Y, Reva B, Goldberg AP, Sander C, Schultz N. 2012. The cBio cancer genomics portal: an open platform for exploring multidimensional cancer genomics data. *Cancer Discov* 2:401–404. <https://doi.org/10.1158/2159-8290.CD-12-0095>.
40. Hast BE, Cloer EW, Goldfarb D, Li H, Siesser PF, Yan F, Walter V, Zheng N, Hayes DN, Major MB. 2014. Cancer-derived mutations in KEAP1 impair NRF2 degradation but not ubiquitination. *Cancer Res* 74:808–817. <https://doi.org/10.1158/0008-5472.CAN-13-1655>.
41. Forbes SA, Beare D, Gunasekaran P, Leung K, Bindal N, Boutselakis H, Ding M, Bamford S, Cole C, Ward S, Kok CY, Jia M, De T, Teague JW, Stratton MR, McDermott U, Campbell PJ. 2015. COSMIC: exploring the world's knowledge of somatic mutations in human cancer. *Nucleic Acids Res* 43:D805–D811. <https://doi.org/10.1093/nar/gku1075>.
42. Forbes SA, Bhamra G, Bamford S, Dawson E, Kok C, Clements J, Menzies A, Teague JW, Futreal PA, Stratton MR. 2008. The Catalogue of Somatic Mutations in Cancer (COSMIC). *Curr Protoc Hum Genet* Chapter 10:Unit 10.11.
43. Levine AJ. 1993. The tumor suppressor genes. *Annu Rev Biochem* 62:623–651. <https://doi.org/10.1146/annurev.bi.62.070193.003203>.
44. Padmanabhan B, Tong KI, Ohta T, Nakamura Y, Scharlock M, Ohtsuiji M, Kang MI, Kobayashi A, Yokoyama S, Yamamoto M. 2006. Structural basis for defects of Keap1 activity provoked by its point mutations in lung cancer. *Mol Cell* 21:689–700. <https://doi.org/10.1016/j.molcel.2006.01.013>.
45. Hayes JD, McMahon M. 2009. NRF2 and KEAP1 mutations: permanent activation of an adaptive response in cancer. *Trends Biochem Sci* 34:176–188. <https://doi.org/10.1016/j.tibs.2008.12.008>.
46. Imielinski M, Berger AH, Hammerman PS, Hernandez B, Pugh TJ, Hodis E, Cho J, Suh J, Capelletti M, Sivachenko A, Sougnez C, Auclair D, Lawrence MS, Stojanov P, Cibulskis K, Choi K, de Waal L, Sharifnia T, Brooks A, Grulich H, Banerji S, Zander T, Seidel D, Leenders F, Ansen S, Ludwig C, Engel-Riedel W, Stoelben E, Wolf J, Goparju C, Thompson K, Winckler W, Kwiatkowski D, Johnson BE, Janne PA, Miller VA, Pao W, Travis WD, Pass HI, Gabriel SB, Lander ES, Thomas RK, Garraway LA, Getz G, Meyerson M. 2012. Mapping the hallmarks of lung adenocarcinoma with massively parallel sequencing. *Cell* 150:1107–1120. <https://doi.org/10.1016/j.cell.2012.08.029>.
47. Berger AH, Brooks AN, Wu X, Shrestha Y, Chouinard C, Piccioni F, Bagul M, Kamburov A, Imielinski M, Hogstrom L, Zhu C, Yang X, Pantel S, Sakai R, Watson J, Kaplan N, Campbell JD, Singh S, Root DE, Narayan R, Natoli T, Lahr DL, Tirosh I, Tamayo P, Getz G, Wong B, Doench J, Subramanian A, Golub TR, Meyerson M, Boehm JS. 2016. High-throughput phenotyping of lung cancer somatic mutations. *Cancer Cell* 30:214–228. <https://doi.org/10.1016/j.ccell.2016.06.022>.
48. Campbell JD, Alexandrov A, Kim J, Wala J, Berger AH, Pedamallu CS, Shukla SA, Guo G, Brooks AN, Murray BA, Imielinski M, Hu X, Ling S, Akbani R, Rosenberg M, Cibulskis C, Ramachandran A, Collisson EA, Kwiatkowski DJ, Lawrence MS, Weinstein JN, Verhaak RG, Wu CJ, Hammerman PS, Cherniack AD, Getz G, Cancer Genome Atlas Research Network, Artyomov MN, Schreiber R, Govindan R, Meyerson M. 2016. Distinct patterns of somatic genome alterations in lung adenocarcinomas and squamous cell carcinomas. *Nat Genet* 48:607–616. <https://doi.org/10.1038/ng.3564>.
49. Valdar WS. 2002. Scoring residue conservation. *Proteins* 48:227–241. <https://doi.org/10.1002/prot.10146>.
50. Capra JA, Singh M. 2007. Predicting functionally important residues from sequence conservation. *Bioinformatics* 23:1875–1882. <https://doi.org/10.1093/bioinformatics/btm270>.
51. Reva B, Antipin Y, Sander C. 2011. Predicting the functional impact of protein mutations: application to cancer genomics. *Nucleic Acids Res* 39:e118. <https://doi.org/10.1093/nar/gkr407>.
52. Walker DR, Bond JP, Tarone RE, Harris CC, Makalowski W, Boguski MS, Greenblatt MS. 1999. Evolutionary conservation and somatic mutation hotspot maps of p53: correlation with p53 protein structural and functional features. *Oncogene* 18:211–218. <https://doi.org/10.1038/sj.onc.1202298>.
53. Bellucci A, Fiorentini C, Zaltieri M, Missale C, Spano P. 2014. The “in situ” proximity ligation assay to probe protein-protein interactions in intact tissues. *Methods Mol Biol* 1174:397–405. [https://doi.org/10.1007/978-1-4939-0944-5\\_27](https://doi.org/10.1007/978-1-4939-0944-5_27).
54. Pacchiana R, Abbate M, Armato U, Dal Pra I, Chiarini A. 2014. Combining immunofluorescence with in situ proximity ligation assay: a novel imaging approach to monitor protein-protein interactions in relation to subcellular localization. *Histochem Cell Biol* 142:593–600. <https://doi.org/10.1007/s00418-014-1244-8>.
55. Zhao Y, Xiong X, Jia L, Sun Y. 2012. Targeting Cullin-RING ligases by MLN4924 induces autophagy via modulating the HIF1-REDD1-TSC1-mTORC1-DEPTOR axis. *Cell Death Dis* 3:e386. <https://doi.org/10.1038/cddis.2012.125>.
56. Luo Z, Pan Y, Jeong LS, Liu J, Jia L. 2012. Inactivation of the Cullin (CUL)-RING E3 ligase by the NEDD8-activating enzyme inhibitor MLN4924 triggers protective autophagy in cancer cells. *Autophagy* 8:1677–1679. <https://doi.org/10.4161/auto.21484>.
57. Egglar AL, Liu G, Pezzuto JM, van Breemen RB, Mesecar AD. 2005. Modifying specific cysteines of the electrophile-sensing human Keap1



- protein is insufficient to disrupt binding to the Nrf2 domain Neh2. *Proc Natl Acad Sci U S A* 102:10070–10075. <https://doi.org/10.1073/pnas.0502402102>.
58. Dinkova-Kostova AT, Kostov RV, Canning P. 2017. Keap1, the cysteine-based mammalian intracellular sensor for electrophiles and oxidants. *Arch Biochem Biophys* 617:84–93. <https://doi.org/10.1016/j.abb.2016.08.005>.
  59. Cleasby A, Yon J, Day PJ, Richardson C, Tickle IJ, Williams PA, Callahan JF, Carr R, Concha N, Kerns JK, Qi H, Sweitzer T, Ward P, Davies TG. 2014. Structure of the BTB domain of Keap1 and its interaction with the triterpenoid antagonist CDDO. *PLoS One* 9:e98896. <https://doi.org/10.1371/journal.pone.0098896>.
  60. Cui W, Bai Y, Luo P, Miao L, Cai L. 2013. Preventive and therapeutic effects of MG132 by activating Nrf2-ARE signaling pathway on oxidative stress-induced cardiovascular and renal injury. *Oxid Med Cell Longev* 2013:306073. <https://doi.org/10.1155/2013/306073>.
  61. Roux KJ, Kim DI, Raida M, Burke B. 2012. A promiscuous biotin ligase fusion protein identifies proximal and interacting proteins in mammalian cells. *J Cell Biol* 196:801–810. <https://doi.org/10.1083/jcb.201112098>.
  62. Kim DI, Birendra KC, Zhu W, Motamedchaboki K, Doye V, Roux KJ. 2014. Probing nuclear pore complex architecture with proximity-dependent biotinylation. *Proc Natl Acad Sci U S A* 111:E2453–E2461. <https://doi.org/10.1073/pnas.1406459111>.
  63. Kim DI, Jensen SC, Noble KA, Kc B, Roux KH, Motamedchaboki K, Roux KJ. 2016. An improved smaller biotin ligase for BioID proximity labeling. *Mol Biol Cell* 27:1188–1196. <https://doi.org/10.1091/mbc.e15-12-0844>.
  64. Ma J, Cai H, Wu T, Sobhian B, Huo Y, Alcivar A, Mehta M, Cheung KL, Ganesan S, Kong AN, Zhang DD, Xia B. 2012. PALB2 interacts with KEAP1 to promote NRF2 nuclear accumulation and function. *Mol Cell Biol* 32:1506–1517. <https://doi.org/10.1128/MCB.06271-11>.
  65. Mulvaney KM, Matson JP, Siesser PF, Tamir TY, Goldfarb D, Jacobs TM, Cloer EW, Harrison JS, Vaziri C, Cook JG, Major MB. 2016. Identification and characterization of MCM3 as a Kelch-like ECH-associated protein 1 (KEAP1) substrate. *J Biol Chem* 291:23719–23733. <https://doi.org/10.1074/jbc.M116.729418>.
  66. Zhang Y, Crouch DH, Yamamoto M, Hayes JD. 2006. Negative regulation of the Nrf1 transcription factor by its N-terminal domain is independent of Keap1: Nrf1, but not Nrf2, is targeted to the endoplasmic reticulum. *Biochem J* 399:373–385. <https://doi.org/10.1042/BJ20060725>.
  67. Tian H, Zhang B, Di J, Jiang G, Chen F, Li H, Li L, Pei D, Zheng J. 2012. Keap1: one stone kills three birds Nrf2, IKKbeta and Bcl-2/Bcl-xL. *Cancer Lett* 325:26–34. <https://doi.org/10.1016/j.canlet.2012.06.007>.
  68. Jiang ZY, Chu HX, Xi MY, Yang TT, Jia JM, Huang JJ, Guo XK, Zhang XJ, You QD, Sun HP. 2013. Insight into the intermolecular recognition mechanism between Keap1 and IKKbeta combining homology modeling, protein-protein docking, molecular dynamics simulations and virtual alanine mutation. *PLoS One* 8:e75076. <https://doi.org/10.1371/journal.pone.0075076>.
  69. Lo SC, Hannink M. 2006. PGAM5, a Bcl-XL-interacting protein, is a novel substrate for the redox-regulated Keap1-dependent ubiquitin ligase complex. *J Biol Chem* 281:37893–37903. <https://doi.org/10.1074/jbc.M606539200>.
  70. Wang Z, Jiang H, Chen S, Du F, Wang X. 2012. The mitochondrial phosphatase PGAM5 functions at the convergence point of multiple necrotic death pathways. *Cell* 148:228–243. <https://doi.org/10.1016/j.cell.2011.11.030>.
  71. Niture SK, Jaiswal AK. 2011. INrf2 (Keap1) targets Bcl-2 degradation and controls cellular apoptosis. *Cell Death Differ* 18:439–451. <https://doi.org/10.1038/cdd.2010.114>.
  72. Niture SK, Jaiswal AK. 2011. Inhibitor of Nrf2 (INrf2 or Keap1) protein degrades Bcl-xL via phosphoglycerate mutase 5 and controls cellular apoptosis. *J Biol Chem* 286:44542–44556. <https://doi.org/10.1074/jbc.M111.275073>.
  73. Niture SK, Jaiswal AK. 2010. Hsp90 interaction with INrf2(Keap1) mediates stress-induced Nrf2 activation. *J Biol Chem* 285:36865–36875. <https://doi.org/10.1074/jbc.M110.175802>.
  74. Chou TF, Li K, Nordin BE, Porubsky P, Frankowski K, Patricelli MP, Aube J, Schoenen FJ, Deshaies R. 2010. Selective, reversible inhibitors of the AAA ATPase p97. Probe reports from the NIH Molecular Libraries Program. National Center for Biotechnology Information, Bethesda, MD.
  75. Chou TF, Brown SJ, Minond D, Nordin BE, Li K, Jones AC, Chase P, Porubsky PR, Stoltz BM, Schoenen FJ, Patricelli MP, Hodder P, Rosen H, Deshaies RJ. 2011. Reversible inhibitor of p97, DBeQ, impairs both ubiquitin-dependent and autophagic protein clearance pathways. *Proc Natl Acad Sci U S A* 108:4834–4839. <https://doi.org/10.1073/pnas.1015312108>.
  76. Chapman E, Maksim N, de la Cruz F, La Clair JJ. 2015. Inhibitors of the AAA+ chaperone p97. *Molecules* 20:3027–3049. <https://doi.org/10.3390/molecules20023027>.
  77. Chou TF, Deshaies RJ. 2011. Development of p97 AAA ATPase inhibitors. *Autophagy* 7:1091–1092. <https://doi.org/10.4161/autophagy.7.9.16489>.
  78. Pickart CM, Cohen RE. 2004. Proteasomes and their kin: proteases in the machine age. *Nat Rev Mol Cell Biol* 5:177–187. <https://doi.org/10.1038/nrm1336>.
  79. Budenholzer L, Cheng CL, Li Y, Hochstrasser M. 2017. Proteasome structure and assembly. *J Mol Biol* <https://doi.org/10.1016/j.jmb.2017.05.027>.
  80. Murata S, Yashiroda H, Tanaka K. 2009. Molecular mechanisms of proteasome assembly. *Nat Rev Mol Cell Biol* 10:104–115. <https://doi.org/10.1038/nrm2630>.
  81. Collins GA, Goldberg AL. 2017. The logic of the 26S proteasome. *Cell* 169:792–806. <https://doi.org/10.1016/j.cell.2017.04.023>.
  82. Ciechanover A, Stanhill A. 2014. The complexity of recognition of ubiquitinated substrates by the 26S proteasome. *Biochim Biophys Acta* 1843:86–96. <https://doi.org/10.1016/j.bbamcr.2013.07.007>.
  83. Mayor T, Lipford JR, Graumann J, Smith GT, Deshaies RJ. 2005. Analysis of polyubiquitin conjugates reveals that the Rpn10 substrate receptor contributes to the turnover of multiple proteasome targets. *Mol Cell Proteomics* 4:741–751. <https://doi.org/10.1074/mcp.M400220-MCP200>.
  84. Verma R, Oania R, Graumann J, Deshaies RJ. 2004. Multiubiquitin chain receptors define a layer of substrate selectivity in the ubiquitin-proteasome system. *Cell* 118:99–110. <https://doi.org/10.1016/j.cell.2004.06.014>.
  85. Elsasser S, Finley D. 2005. Delivery of ubiquitinated substrates to protein-unfolding machines. *Nat Cell Biol* 7:742–749. <https://doi.org/10.1038/ncb0805-742>.
  86. Yamamoto T, Suzuki T, Kobayashi A, Wakabayashi J, Maher J, Motohashi H, Yamamoto M. 2008. Physiological significance of reactive cysteine residues of Keap1 in determining Nrf2 activity. *Mol Cell Biol* 28:2758–2770. <https://doi.org/10.1128/MCB.01704-07>.
  87. Proctor EA, Dokholyan NV. 2016. Applications of Discrete Molecular Dynamics in biology and medicine. *Curr Opin Struct Biol* 37:9–13. <https://doi.org/10.1016/j.sbi.2015.11.001>.
  88. Proctor EA, Ding F, Dokholyan NV. 2011. Discrete molecular dynamics. *Wiley Interdiscip Rev Comput Mol Sci* 1:80–92. <https://doi.org/10.1002/wcms.4>.
  89. Shirvanyants D, Ding F, Tsao D, Ramachandran S, Dokholyan NV. 2012. Discrete molecular dynamics: an efficient and versatile simulation method for fine protein characterization. *J Phys Chem B* 116:8375–8382. <https://doi.org/10.1021/jp2114576>.
  90. Ding F, Dokholyan NV. 2005. Simple but predictive protein models. *Trends Biotechnol* 23:450–455. <https://doi.org/10.1016/j.tibtech.2005.07.001>.
  91. Fontana A, de Laureto PP, Spolaore B, Frare E, Picotti P, Zamboni M. 2004. Probing protein structure by limited proteolysis. *Acta Biochim Pol* 51:299–321.
  92. Moehlenkamp JD, Johnson JA. 1999. Activation of antioxidant/electrophile-responsive elements in IMR-32 human neuroblastoma cells. *Arch Biochem Biophys* 363:98–106. <https://doi.org/10.1006/abbi.1998.1046>.
  93. Morimoto T, Tashiro Y, Matsuura S. 1967. Chase of newly synthesized proteins in guinea-pig pancreas with cycloheximide. *Biochim Biophys Acta* 138:631–633. [https://doi.org/10.1016/0005-2787\(67\)90567-9](https://doi.org/10.1016/0005-2787(67)90567-9).
  94. Eftekharzadeh B, Maghsoudi N, Khodagholfi F. 2010. Stabilization of transcription factor Nrf2 by tBHQ prevents oxidative stress-induced amyloid beta formation in NT2N neurons. *Biochimie* 92:245–253. <https://doi.org/10.1016/j.biochi.2009.12.001>.
  95. Fink AL. 1998. Protein aggregation: folding aggregates, inclusion bodies and amyloid. *Fold Des* 3:R9–R23. [https://doi.org/10.1016/S1359-0278\(98\)00002-9](https://doi.org/10.1016/S1359-0278(98)00002-9).
  96. Mizushima N. 2007. Autophagy: process and function. *Genes Dev* 21:2861–2873. <https://doi.org/10.1101/gad.1599207>.
  97. Mizushima N, Komatsu M. 2011. Autophagy: renovation of cells and tissues. *Cell* 147:728–741. <https://doi.org/10.1016/j.cell.2011.10.026>.
  98. Mizushima N. 2010. Autophagy. *FEBS Lett* 584:1279. <https://doi.org/10.1016/j.febslet.2010.02.053>.

99. Yin Z, Pascual C, Klionsky DJ. 2016. Autophagy: machinery and regulation. *Microb Cell* 3:588–596. <https://doi.org/10.15698/mic2016.12.546>.
100. Komatsu M, Kurokawa H, Waguri S, Taguchi K, Kobayashi A, Ichimura Y, Sou YS, Ueno I, Sakamoto A, Tong KI, Kim M, Nishito Y, Iemura S, Natsume T, Ueno T, Kominami E, Motohashi H, Tanaka K, Yamamoto M. 2010. The selective autophagy substrate p62 activates the stress responsive transcription factor Nrf2 through inactivation of Keap1. *Nat Cell Biol* 12:213–223. <https://doi.org/10.1038/ncb2021>.
101. Lau A, Wang XJ, Zhao F, Villeneuve NF, Wu T, Jiang T, Sun Z, White E, Zhang DD. 2010. A noncanonical mechanism of Nrf2 activation by autophagy deficiency: direct interaction between Keap1 and p62. *Mol Cell Biol* 30:3275–3285. <https://doi.org/10.1128/MCB.00248-10>.
102. Stepkowski TM, Kruszewski MK. 2011. Molecular cross-talk between the NRF2/KEAP1 signaling pathway, autophagy, and apoptosis. *Free Radic Biol Med* 50:1186–1195. <https://doi.org/10.1016/j.freeradbiomed.2011.01.033>.
103. Taguchi K, Fujikawa N, Komatsu M, Ishii T, Unno M, Akaike T, Motohashi H, Yamamoto M. 2012. Keap1 degradation by autophagy for the maintenance of redox homeostasis. *Proc Natl Acad Sci U S A* 109:13561–13566. <https://doi.org/10.1073/pnas.1121572109>.
104. Kirkin V, Lamark T, Sou YS, Bjorkoy G, Nunn JL, Bruun JA, Shvets E, McEwan DG, Clausen TH, Wild P, Bilusic I, Theurillat JP, Overvatn A, Ishii T, Elazar Z, Komatsu M, Dikic I, Johansen T. 2009. A role for NBR1 in autophagosomal degradation of ubiquitinated substrates. *Mol Cell* 33:505–516. <https://doi.org/10.1016/j.molcel.2009.01.020>.
105. Lippai M, Low P. 2014. The role of the selective adaptor p62 and ubiquitin-like proteins in autophagy. *Biomed Res Int* 2014:832704.
106. Ichimura Y, Waguri S, Sou YS, Kageyama S, Hasegawa J, Ishimura R, Saito T, Yang Y, Kouno T, Fukutomi T, Hoshii T, Hirao A, Takagi K, Mizushima T, Motohashi H, Lee MS, Yoshimori T, Tanaka K, Yamamoto M, Komatsu M. 2013. Phosphorylation of p62 activates the Keap1-Nrf2 pathway during selective autophagy. *Mol Cell* 51:618–631. <https://doi.org/10.1016/j.molcel.2013.08.003>.
107. Jiang X, Bao Y, Liu H, Kou X, Zhang Z, Sun F, Qian Z, Lin Z, Li X, Liu X, Jiang L, Yang Y. 2017. VPS34 stimulation of p62 phosphorylation for cancer progression. *Oncogene* <https://doi.org/10.1038/ncr.2017.295>.
108. Yoshii SR, Mizushima N. 2017. Monitoring and measuring autophagy. *Int J Mol Sci* 18:1865. <https://doi.org/10.3390/ijms18091865>.
109. Banani SF, Lee HO, Hyman AA, Rosen MK. 2017. Biomolecular condensates: organizers of cellular biochemistry. *Nat Rev Mol Cell Biol* 18:285–298. <https://doi.org/10.1038/nrm.2017.7>.
110. Hyman AA, Weber CA, Julicher F. 2014. Liquid-liquid phase separation in biology. *Annu Rev Cell Dev Biol* 30:39–58. <https://doi.org/10.1146/annurev-cellbio-100913-013325>.
111. Klionsky DJ, Baehrecke EH, Brummel JH, Chu CT, Codogno P, Cuervo AM, Debnath J, Deretic V, Elazar Z, Eskelinen EL, Finkbeiner S, Fueyo-Margareto J, Gewirtz D, Jaattela M, Kroemer G, Levine B, Melia TJ, Mizushima N, Rubinsztein DC, Simonsen A, Thorburn A, Thumm M, Tooze SA. 2011. A comprehensive glossary of autophagy-related molecules and processes (2nd edition). *Autophagy* 7:1273–1294. <https://doi.org/10.4161/auto.7.11.17661>.
112. Jiang T, Chen N, Zhao F, Wang XJ, Kong B, Zheng W, Zhang DD. 2010. High levels of Nrf2 determine chemoresistance in type II endometrial cancer. *Cancer Res* 70:5486–5496. <https://doi.org/10.1158/0008-5472.CAN-10-0713>.
113. Shibata T, Kokubu A, Gotoh M, Ojima H, Ohta T, Yamamoto M, Hirohashi S. 2008. Genetic alteration of Keap1 confers constitutive Nrf2 activation and resistance to chemotherapy in gallbladder cancer. *Gastroenterology* 135:1358–1368.e4. <https://doi.org/10.1053/j.gastro.2008.06.082>.
114. Choi B-H, Kwak M-K. 2016. Shadows of NRF2 in cancer: resistance to chemotherapy. *Curr Opin Toxicol* 1:20–28. <https://doi.org/10.1016/j.cotox.2016.08.003>.
115. Lee YS, Yoon S, Park MS, Kim JH, Lee JH, Song CW. 2010. Influence of p53 expression on sensitivity of cancer cells to bleomycin. *J Biochem Mol Toxicol* 24:260–269. <https://doi.org/10.1002/jbt.20334>.
116. Shibata T, Ohta T, Tong KI, Kokubu A, Odogawa R, Tsuta K, Asamura H, Yamamoto M, Hirohashi S. 2008. Cancer related mutations in NRF2 impair its recognition by Keap1-Cul3 E3 ligase and promote malignancy. *Proc Natl Acad Sci U S A* 105:13568–13573. <https://doi.org/10.1073/pnas.0806268105>.
117. Katsuoka F, Yamazaki H, Yamamoto M. 2016. Small Maf deficiency recapitulates the liver phenotypes of Nrf1- and Nrf2-deficient mice. *Genes Cells* 21:1309–1319. <https://doi.org/10.1111/gtc.12445>.
118. Dao TP, Kolaitis RM, Kim HJ, O'Donovan K, Martyniak B, Colicino E, Hehrl H, Taylor JP, Castaneda CA. 2018. Ubiquitin modulates liquid-liquid phase separation of UBLN2 via disruption of multivalent interactions. *Mol Cell* 69:965–978.e6. <https://doi.org/10.1016/j.molcel.2018.02.004>.
119. Bergeron-Sandoval LP, Safaei N, Michnick SW. 2016. Mechanisms and consequences of macromolecular phase separation. *Cell* 165:1067–1079. <https://doi.org/10.1016/j.cell.2016.05.026>.
120. Kageyama S, Sou YS, Uemura T, Kametaka S, Saito T, Ishimura R, Kouno T, Bedford L, Mayer RJ, Lee MS, Yamamoto M, Waguri S, Tanaka K, Komatsu M. 2014. Proteasome dysfunction activates autophagy and the Keap1-Nrf2 pathway. *J Biol Chem* 289:24944–24955. <https://doi.org/10.1074/jbc.M114.580357>.
121. Liu WJ, Ye L, Huang WF, Guo LJ, Xu ZG, Wu HL, Yang C, Liu HF. 2016. p62 links the autophagy pathway and the ubiquitin-proteasome system upon ubiquitinated protein degradation. *Cell Mol Biol Lett* 21:29. <https://doi.org/10.1186/s11658-016-0031-z>.
122. Seguin SJ, Morelli FF, Vinet J, Amore D, De Biasi S, Poletti A, Rubinsztein DC, Carra S. 2014. Inhibition of autophagy, lysosome and VCP function impairs stress granule assembly. *Cell Death Differ* 21:1838–1851. <https://doi.org/10.1038/cdd.2014.103>.
123. Peng H, Yang J, Li G, You Q, Han W, Li T, Gao D, Xie X, Lee BH, Du J, Hou J, Zhang T, Rao H, Huang Y, Li Q, Zeng R, Hui L, Wang H, Xia Q, Zhang X, He Y, Komatsu M, Dikic I, Finley D, Hu R. 2017. Ubiquitylation of p62/sequestosome1 activates its autophagy receptor function and controls selective autophagy upon ubiquitin stress. *Cell Res* 27:657–674. <https://doi.org/10.1038/cr.2017.40>.
124. Lee Y, Chou TF, Pittman SK, Keith AL, Razani B, Weihl CC. 2017. Keap1/Cullin3 modulates p62/SQSTM1 activity via UBA domain ubiquitination. *Cell Rep* 20:1994. <https://doi.org/10.1016/j.celrep.2017.08.019>.
125. Zaffagnini G, Savova A, Danieli A, Romanov J, Tremel S, Ebner M, Peterbauer T, Sztacho M, Trapannone R, Tarafder AK, Sachse C, Martens S. 20 July 2018. Phasing out the bad—how SQSTM1/p62 sequesters ubiquitinated proteins for degradation by autophagy. *Autophagy* <https://doi.org/10.1080/15548627.2018.1462079>.
126. Zaffagnini G, Savova A, Danieli A, Romanov J, Tremel S, Ebner M, Peterbauer T, Sztacho M, Trapannone R, Tarafder AK, Sachse C, Martens S. 2018. p62 filaments capture and present ubiquitinated cargos for autophagy. *EMBO J* 37:e98308. <https://doi.org/10.15252/emboj.201798308>.
127. Sun D, Wu R, Zheng J, Li P, Yu L. 2018. Polyubiquitin chain-induced p62 phase separation drives autophagic cargo segregation. *Cell Res* 28:405–415. <https://doi.org/10.1038/s41422-018-0017-7>.
128. Chen PH, Smith TJ, Wu J, Siesser PF, Bisnett BJ, Khan F, Hogue M, Soderblom E, Tang F, Marks JR, Major MB, Swarts BM, Boyce M, Chi JT. 2017. Glycosylation of KEAP1 links nutrient sensing to redox stress signaling. *EMBO J* 36:2233–2250. <https://doi.org/10.15252/emboj.201696113>.
129. Allalou A, Wahlby C. 2009. BlobFinder, a tool for fluorescence microscopy image cytometry. *Comput Methods Programs Biomed* 94:58–65. <https://doi.org/10.1016/j.cmpb.2008.08.006>.
130. Cox J, Mann M. 2008. MaxQuant enables high peptide identification rates, individualized p.p.b.-range mass accuracies and proteome-wide protein quantification. *Nat Biotechnol* 26:1367–1372. <https://doi.org/10.1038/nbt.1511>.
131. Tyanova S, Temu T, Carlson A, Sinitcyn P, Mann M, Cox J. 2015. Visualization of LC-MS/MS proteomics data in MaxQuant. *Proteomics* 15:1453–1456. <https://doi.org/10.1002/pmic.201400449>.
132. The UniProt Consortium. 2017. UniProt: the universal protein knowledgebase. *Nucleic Acids Res* 45:D158–D169. <https://doi.org/10.1093/nar/gkw1099>.
133. Tyanova S, Temu T, Sinitcyn P, Carlson A, Hein MY, Geiger T, Mann M, Cox J. 2016. The Perseus computational platform for comprehensive analysis of (prote)omics data. *Nat Methods* 13:731–740. <https://doi.org/10.1038/nmeth.3901>.
134. Vizcaino JA, Csordas A, del-Toro N, Dianas JA, Griss J, Lavidas I, Mayer G, Perez-Riverol Y, Reisinger F, Ternent T, Xu QW, Wang R, Hermjakob H. 2016. 2016 update of the PRIDE database and its related tools. *Nucleic Acids Res* 44:D447–D456. <https://doi.org/10.1093/nar/gkv1145>.
135. Madden TL, Tatusov RL, Zhang J. 1996. Applications of network BLAST server. *Methods Enzymol* 266:131–141. [https://doi.org/10.1016/S0076-6879\(96\)66011-X](https://doi.org/10.1016/S0076-6879(96)66011-X).
136. Pei J, Kim BH, Grishin NV. 2008. PROMALS3D: a tool for multiple protein sequence and structure alignments. *Nucleic Acids Res* 36:2295–2300. <https://doi.org/10.1093/nar/gkn072>.